Electronic Theses and Dissertations   Retrospective theses

2002

Optically-excited excitonic states in semiconductor superlattices

Lachaine, Jean-Marc

Optically-Excited Excitonic States in Semiconductor Superlattices

by

Jean-Marc Lachaîne ©

Submitted to the Physics Department in partial

fulfillment of the requirements for the degree of

Master of Science

Lakehead University

Thunder Bay, Ontario

August, 2002

National Library
of Canada

Bibliothèque nationale
du Canada

Acquisitions and
Bibliographic Services

Acquisisitons et
services bibliographiques

395 Wellington Street
Ottawa ON K1A 0N4
Canada

395, rue Wellington
Ottawa ON K1A 0N4
Canada

The author has granted a non-exclusive licence allowing the National Library of Canada to reproduce, loan, distribute or sell copies of this thesis in microform, paper or electronic formats.

The author retains ownership of the copyright in this thesis. Neither the thesis nor substantial extracts from it may be printed or otherwise reproduced without the author's permission.

L'auteur a accordé une licence non exclusive permettant à la Bibliothèque nationale du Canada de reproduire, prêter, distribuer ou vendre des copies de cette thèse sous la forme de microfiche/film, de reproduction sur papier ou sur format électronique.

L'auteur conserve la propriété du droit d'auteur qui protège cette thèse. Ni la thèse ni des extraits substantiels de celle-ci ne doivent être imprimés ou aturement reproduits sans son autorisation.

Canada

Acknowledgements

The author would like to express his sincerest thanks and appreciation to, in particular, M. Dignam and M. Hawton for the many invaluable discussions and, in general, to the Physics faculty at Lakehead University for their continuing support. Also, this thesis would not have been possible had it not been for the patience, support and encouragement of the author's wife, Julie.

Je dédie cette thèse à la mémoire de mes parents
J.E. Bernard Lachaîne et M.A. Carmen Turgeon
Soyez fiers de moi.

Optically-Excited Excitonic States in Semiconductor Superlattices

by

Jean-Marc Lachaîne

Submitted to the Physics Department
on 7 August, 2002, in partial fulfillment of the
requirements for the degree of
Master of Science

Abstract

An efficient method for calculation of the exciton states in type-I superlattices is developed and demonstrated. The model, based on the work of Dignam & Sipe [Phys. Rev. B **43**, 4097 (1991)] , includes bound and quasi-continuous two-well exciton eigenstates as a basis in which to expand the superlattice exciton eigenstates. This basis is used to calculate the excitonic absorption spectra for two different type-I superlattices as a function of the applied static field. The results are found to be in very good agreement with the experimental results of Holfeld *et. al* [Phys. Rev. Lett. **81**, 874 (1998)] for the 67Å/17Å superlattice and with those of Agulló-Rueda *et. al* [Phys. Rev. B **41**, 1676 (1990)] for the 40Å/40 Å superlattice. On the basis of these results, this method should be ideal for use in the calculation of nonlinear and coherent effects in optically excited semiconductor superlattices.

Thesis Supervisor: Marc Dignam
Title: Assistant Professor, Department of Physics, Queen's University

2

Chapter 1

ι

Introduction

The importance of semiconducting devices in current technology cannot be overstated. The widespread use of devices ranging from transistors to semiconductor lasers has lead to the word *"semiconductor"* becoming a part of the household vernacular. In this thesis we consider a very specific type of periodic quantum well semiconductor structure commonly referred to as a superlattice. Quantum well and superlattice devices have been the subject of ever increasing interest for over 20 years. In addition to their potential technological applications, these structures have great deal of interesting physics to reveal.

Superlattices are structures that are made up of two types of semiconducting material, one type that acts as a quantum *well* and the other acting as a quantum *barrier.*
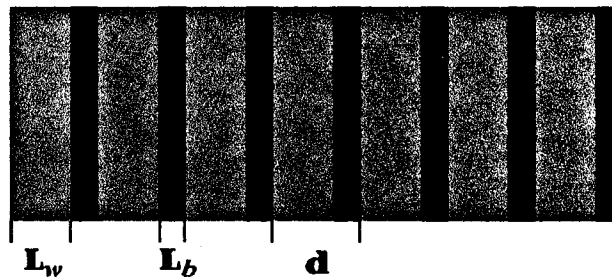
Figure 1-1: Two-dimensional schematic of a semiconductor superlattice. Superlattices can have equal or different well (L_w) and barrier (L_b) widths. The superlattice period is defined

$$d \equiv L_w + L_b \ .$$

The structures are grown by alternating the well and barrier material such that the layers

3

of well material are all of width L_w and the barrier layers are all of width L_b. The superlattice is thus a periodic structure with period $d = L_w + L_d$ (see Figure 1-1).

Superlattices come predominately in two types. In the so-called "type-I" superlattice, where electrons and holes are confined to the same layers, is exemplified by the $GaAs/Al_xGa_{1-x}As$ lattice for $x < 0.4$. In "type-II" superlattices, the electrons and holes are confined to different layers. One example of a type-II superlattice's composition is $GaAs/AlAs$. This combination of semiconducting compounds exhibits type-II behaviour for narrow GaAs well widths. However, when the well widths are wide, a $GaAs/AlAs$ superlattice exhibits type-I behaviour.

The initial work that provided much of the stimulus towards the eventual creation of a superlattice occurred nearly 80 years ago. At that time Bloch predicted that electronic wavepackets in a periodic structure subjected to an external electric field would undergo oscillations [1] . It would take many years before the first experimental evidence [2] , of what has come to be known as "Bloch Oscillations" (BO), proved Bloch's prediction to be true. Nearly two decades after the publication of this pioneering work, James'[4] investigations of the effect of a uniform electric field on electrons in a crystal predicted the possible quantization of the electronic energy spectrum in the direction of the field. Then, some 32 years after Bloch's ground-breaking paper, Wannier theorized that the energy spectrum of a so-called "Bloch electron", when subjected to an electric field, should consist of equally spaced energy levels. He further suggested that the energy spacing, eFd should depend only on the field F and the periodicity of the crystal d. The energy splitting predicted by Wannier is analogous to the Stark effect, so-named for the electric field induced splitting of the hydrogen Balmer series observed by Stark in 1913. This gives rise to the name "Wannier-Stark Ladder" (WSL) which is used to signify the energy spectrum of a particle in a periodic structure that is subjected to an electric field.

The WSL can be viewed as the frequency-space analogue to BO. Both are general properties that can be applied to any periodic structure in the presence of an external field. Initially predicted for natural crystals, it was not until the proposal of Esaki and Tsu in 1970 that any hope of observing these phenomena existed [5] . This is because, in natural crystals, the period of the Bloch oscillations is much longer than the lifetime of the Wannier-Stark states. What Esaki & Tsu proposed was to study the properties of artificial periodic superlattice structures, whose period could be tailor-made to allow for the observation of the WSL and of BO. The first

4

experiments however, conducted on multiple-quantum-well structures [6] , showed no evidence of either the WSL or BO. Moreover, the results of these experiments were well described in terms of single isolated quantum wells [10] . It was not until 1988 that experiments performed using photoluminescence, photocurrent, and photoluminescence excitation spectroscopy provided the first real evidence of the WSL [11] . Experimental evidence of BO followed a few years later using four-wave mixing techniques [2],[12] .

The experimental picture has benefited from increasing sample quality stemming from the inevitable improvement in epitaxial growth methods and from increasing experimental sophistication. These improvements have allowed a more detailed analysis of the absorption spectra, leading to, for example, the observation [47] of theoretically predicted [13],[15] Fano resonances [16] . The theoretical successes, however, have come amidst debate and some controversy.

The physical system presented by a superlattice structure is a complex one. To the best of the author's knowledge, there has been no exact theoretical description of the electronic and optical properties of superlattices. There have, however, been a number of useful approximate models presented. These have had some successes at either predicting or reproducing experimental results. But, accompanying the very important theoretical research, there has occurred no small measure of controversy.

Wannier, in his 1960 paper [3] , along with predicting the WSL, suggested that the eigenfunctions for a Bloch electron in the presence of an external electric field would not be normalizable thus leading to the conclusion that they would not be localized states. A few years later, in 1968, Zak contested the very existence of the ladder. As noted above, it would take 20 years until experimental evidence supported Wannier's prediction. Controversy, however, did not end with merely questioning the existence of the WSL.

Most of the early theoretical work concentrated on the *single-particle problem*. The most common single-particle model of the opto-electronic properties of a superlattice is essentially a nearest-neighbour tight-binding modelling of electron envelope functions. Most descriptions that use this model consider a single miniband and neglect the coupling between superlattice minibands [18] , or assume a finite number of minibands [19] . In tight-binding, the former leads to a zero field, discrete energy spectrum. This is the crux of the so-called "*Wannier-Stark Controversy*". The controversy questions the validity of describing the physics using localized

5

wavefunctions.

In the single-miniband single-particle tight-binding model, neglecting wavefunction overlap, all but nearest-neighbour potential-overlap, and quantum confined Stark effects, the superlattice energy levels are given by

$$E_n = E_0 + eFnd , \qquad (1.1)$$

where E_0 is approximately the energy of a particle in the potential of a single site, e is the modulus of the electronic charge, F is the field, d is the superlattice period, and n is an integer [20] . This relationship leads to a single-particle version of the familiar fan shape of the WSL as shown in Figure 1-2.

Single Particle WSL
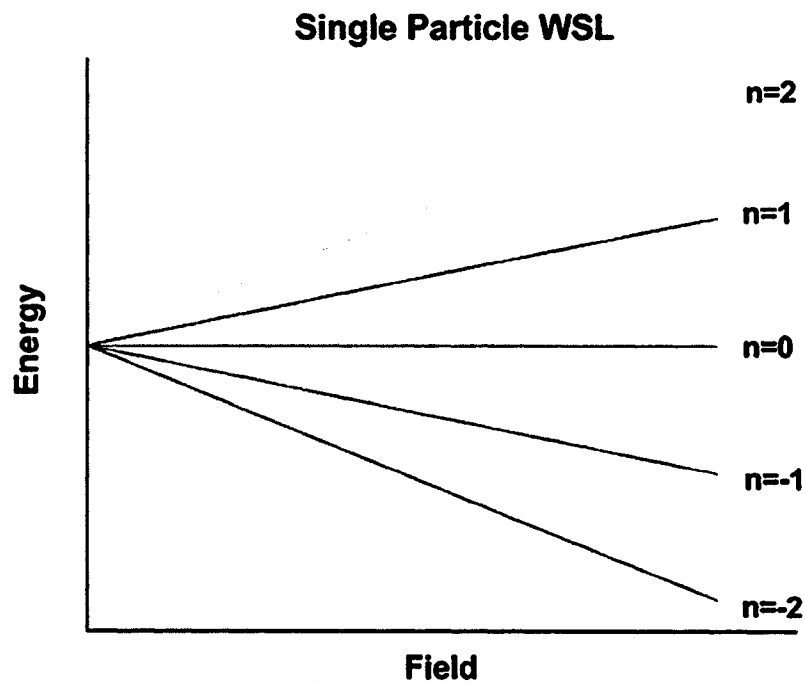
Figure 1-2: Schematic plot of a single-particle Wannier-Stark Ladder.

The WSL eigenstates determined using this model are stationary states that are localized about the lattice sites $z = nd$. The localization length for these eigenstates is of order $L =$

6

$\Delta / (2eF)$, where Δ is the miniband width. In Figure 1-3 we show a schematic of two superlattice energy bands under the influence of an applied static field and include the localization length parameters. The electric field shifts the bands such that they gain a slope given by eF.
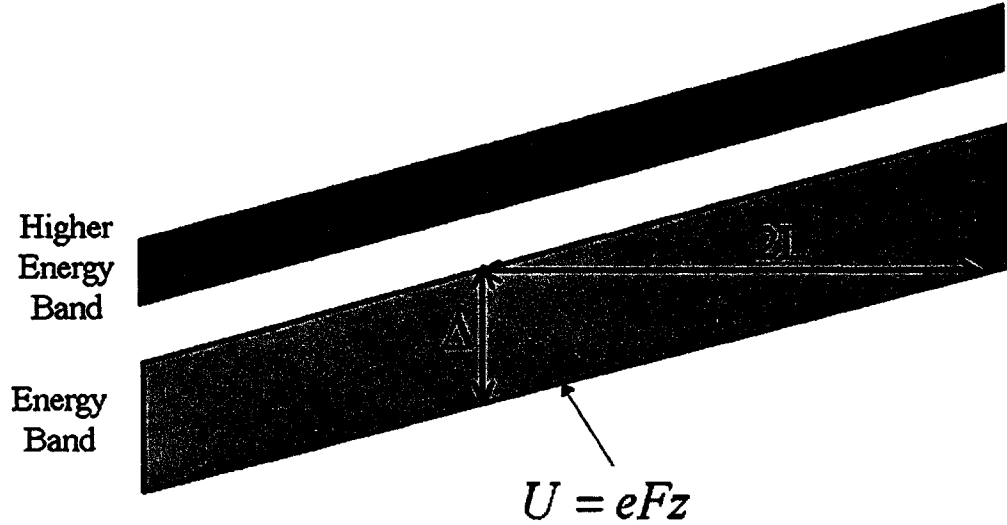
Figure 1-3: Schematic showing localization length parameters.

Localization can then be understood as arising from a decoupling of the energy levels of the separate wells that make up the superlattice. This decoupling is due to the field imposed interwell energy shift of eFd. Consequently, the probability of interwell tunnelling is drastically reduced thus leading to eigenstates, given by

$$\chi_n(z) = \sum_p J_{n-p}\left(\frac{L}{d}\right) f(z - pd) \tag{1.2}$$

where $J_{n-p}\left(\frac{L}{d}\right)$ is a Bessel function of integer order $n - p$ and $f(z - pd)$ is the eigenstate of a particle in the potential of a single site [20] . Figure 4 shows a typical single-particle wavefunction. Localization occurs over a few adjacent wells. We have also shown the field induced energy splitting, eFd, between the wells and have provided a schematic of $f(z - pd)$.

7
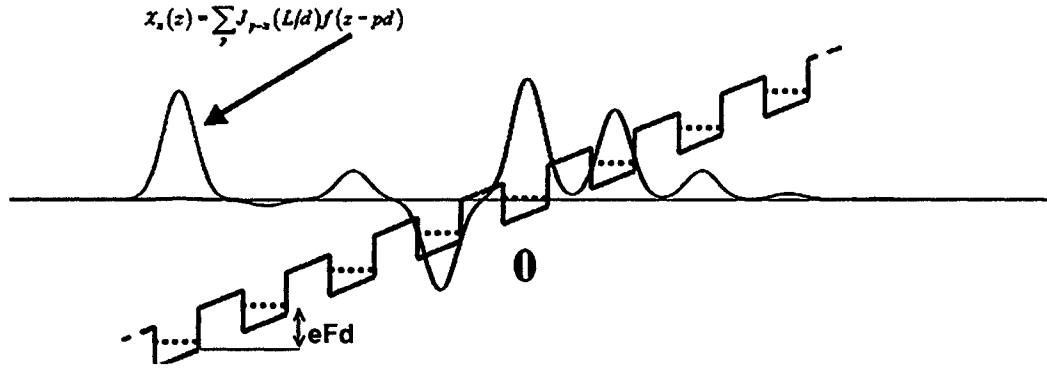
Figure 1-4: Single-particle states are localized over a few adjacent wells. Here the curve in black is the wavefunction of a particle in the potential of a single site. The curve in red is the single-particle wavefunction.

Nearly every model to date, including the one to be presented here, begins with the assumption of an infinite superlattice. It speaks to the complexity of the problem that one considers an infinite system to be a simplification. Under this assumption, the reason for the controversy can be understood in a simple intuitive way. A superlattice can be viewed as a series of discrete quantum wells. When the barrier widths are narrow enough, as is the case for most superlattices of interest, the discrete single well states couple with those in neighbouring wells by tunnelling. Thus the discrete single well energies broaden into the so-called "superlattice minibands". When a static electric field is applied, we obtain the localized states of the WSL as described above if coupling between minibands is neglected (as shown in Figures 1-3 and 1-4). However Zener tunnelling can occur when inter-miniband coupling is accounted for [21] . Zener tunnelling between the minibands gives rise to completely delocalized states. The probability of tunnelling across the miniband gap is given approximately by [22]

$$ P = \exp\left[-\left(\frac{mdE_{gap}^2}{2\hbar^2 eF} \right) \right] , \qquad (1.3) $$

where E_{gap} is the energy separation between the minibands and m is the particle mass. Thus, when the miniband separation is greater than eFd, where d is the superlattice period, the minibands are essentially decoupled and the effect of the inter-miniband tunnelling can be neglected [13][15] . This is the case for most of the superlattice structures that have been investigated to date. For the structures being considered here, the probability of tunnelling out

8

of the first miniband is less than 10^{-20}. These structures can be well described using one-band models.

All experiments that have observed the WSL are optical experiments. One of the most accurate and versatile experimental methods used is photocurrent spectroscopy where the sample is illuminated by a monochromatic source, thereby photo-exciting carriers with an energy given by the photon energy. Changes in the photo-induced current are then measured as a function of photon energy, providing a picture of the structure's absorption spectrum. Two other commonly used experimental methods, photoluminescence and photoluminescence excitation spectroscopy are also performed by exciting the sample using monochromatic sources at a specific frequency. Once the source is extinguished, the sample is scanned and the intensity of the emitted light is measured. Direct absorption measurements, where a sample is illuminated with light of a known spectral composition which is then compared to the spectral composition of the transmitted light, are also used. Clearly all of these methods share a common thread. They are all based on photo-exciting the samples. Photo-exciting semiconductors leads to the creation of electron-hole pairs.

Single-particle models, as applied to optically excited electron-hole pairs, for the most part, suffer from the same failing. They ignore the Coulomb interaction between electrons and holes. It is a widely accepted tenet of condensed matter physics that an optically excited semiconductor electron will couple with the hole left behind in the valence band. The Coulomb-coupled electron-hole pair form a hydrogenic quasi-particle commonly referred to as an exciton. Thus it is the absorption spectrum of the *exciton* Wannier-Stark ladder that is measured experimentally. This leads to the conclusion that, in order to adequately describe the experimental evidence, the excitonic energy levels must be calculated. There are effectively two approaches to the calculation of excitonic states in a superlattice. The first, and most common, employs a basis of free electron-hole states. The second approach is to employ a basis of correlated electron-hole pair states, that is, an excitonic basis.

Recently, Glutsch and Bechstedt presented a model where they, in their own words,"... perform a highly accurate calculation of the single-particle eigenstates, which gives important insight in the nature of the localized states and is a key result towards resolving the Wannier-Stark controversy..." [25] . Though these authors present a number of results based on separate

9

single particle eigenfunctions for the electron and hole, their calculated absorption spectra are determined using an excitonic Hamiltonian operating on *two-particle eigenstates* constructed from non-interacting electron and hole wavefunctions [25],[26] . The numerical method used by Glutsch and Bechstedt involves a finite difference discretization in both time and space of the time-dependent Schrödinger equation. The Schrödinger equation is then solved simultaneously with a discretized version of the equation for the optical susceptibility in order to determine the susceptibility. This provides the superlattice absorption spectrum for a given applied static field since the absorption varies as the imaginary part of the susceptibility. Reference [24] contains an extensive description of this method. Though this method lends itself well to a variety of structures (single well to superlattices), under a number of different conditions (electric and magnetic fields, rough interfaces), it only provides optical spectra.

In similar manner to the approach used by Glutsch and Bechstedt, there are a number of authors who use non-interacting electron and hole wavefunctions as a basis for the excitonic states in a superlattice [27]-[31] . Though some of these are very accurate when valence band mixing is taken into account [27]-[29] , these models require numerous and involved matrix element calculations. It has been suggested that the number ($\sim 10^6$) of basis functions required in these calculations can lead to matrices that cannot be solved using standard eigenroutines [32] .

A model, presented by Linder [15] , using single-particle localized Kane functions as a basis in which to expand the excitonic Hamiltonian, has successfully predicted Fano resonances and has provided absorption spectra that reproduced the experimental results of Agulló-Rueda *et. al* [48] . Linder's method, however, suffers from a *low-field limit*. His model requires increasing numbers of basis states with decreasing field strength effectively imposing a lower bound on the fields for which accurate results are returned. For example, in reference [15] , Linder states that the lowest field accessible to his method for a 11/1 ML (11 monolayer wells and 1 monolayer barriers: 1 monolayer $\approx$ 12.2 Å for GaAs) is 33 kV/cm. His method requires 5000 basis states at this field. For zero-field, the Linder model fails, and the Kane states need to be replaced by Wannier states in order to provide results that are in agreement with experiment. It is important to note that Linder covers a broader photon energy range in his calculations than is considered here. In order to cover such a range using the model to be presented, we would

10

be required to increase the number basis states used. However, this increase would amount to a need to include about 100 basis states for calculations at all field strengths. It is also important to note that the theoretical spectra shown by Linder have been broadened using a field-dependent FWHM ranging from 20 meV to 80 meV. The significance of these widths will become clear further in this document. As a final note, Linder's method, like that of Glutsch et. al [24] , provides only linear optical absorption.

A theoretical model, presented by Whittaker, that also successfully predicted Fano resonances and provided accurate absorption spectra, uses single-particle Wannier functions as a basis [13] . This model is similar to those of Glutsch et. al and Linder in the sense that the optical absorption is determined by solving a set of coupled differential equations. The solutions return good estimates for the optical spectra, however, the method provides no information about the states themselves. Although all of the models we have discussed successfully calculate the optical spectra, they are either too time-consuming or otherwise unsuited to the calculation of coherent and nonlinear optical effects. Such effects are best treated in an excitonic basis [14] .

To the best knowledge of the author, the only theoretical models to use a purely excitonic basis for the superlattice were provided by Whittaker [33] and Dignam & Sipe [39], [40] . The later workers used a tight-binding of excitonic two-well ground (1S) states to form the superlattice exciton wave function. Though the results of this model provided insight into the physics of the superlattice excitons, the model fails to include states of higher in-plane energy. Although much of the physics can be understood without the higher continuum states, these states have been shown to be important in describing the full absorption spectrum including the Fano resonances.

This thesis presents an excitonic model for the superlattice that is based on the work of Dignam & Sipe (DS). The model presented includes states of higher in-plane energy. In a manner similar to DS we expand the superlattice Hamiltonian into a tight-binding of excitonic Two-Well states. A major difference in our method compared to that of DS is that we include in our two-well states, both bound and quasi-continuum in-plane states. The method is sufficiently simple and efficient that it can be used as a first step in the calculation of coherent and nonlinear optical effects in superlattices excited by ultra-short (100 fs) optical pulses.

11

The structure of this thesis is as follows: In Chapter II, we present the theory. In Chapter III we present our results and analysis. Finally in Chapter IV we summarize our findings.

12

Chapter 2

Theory

This thesis considers optically excited excitonic states in GaAs/Ga$_{1-x}$Al$_x$As superlattices. These structures are type I superlattices where both electrons and holes are largely confined to the GaAs layers. When such superlattices are optically excited by photons with energies near that of the bandgap, electron-hole pairs are created. These pairs may be bound, that is, have energy lower than the non-interacting electron-hole pair ground-state, or may be unbound. We refer to all of these pairs as excitons.

In bulk GaAs, the heavy-hole and light-hole bands are degenerate at the Γ point. However, in quantum wells and multiple quantum well structures, such as superlattices, the degeneracy disappears and sets of heavy- and light-hole levels are created[37]. In this work we will consider heavy-hole excitons, although the formalism is equally valid for light-hole excitons.

In principle, the calculation of the excitonic states in superlattices should include the mixing that arises between the light- and heavy-hole sub-bands [38]. The non-parabolicity of the conduction band should also be included in such a treatment. However, near the band edge, dispersion is nearly parabolic [36]. Therefore, since we are interested only in optically accessible states, for which the centre of mass wavevector is zero, band non-parabolicity is ignored. It has been shown that ignoring both non-parabolicity and valence band mixing can lead to errors of $\lesssim 0.7$ meV (roughly 10%) in the binding energy of the heavy-hole excitons [37]. Thus, in what follows, we work in the "axial model" of the envelope function approximation [35] and for simplicity, ignore valence band mixing and band non-parabolicity.

13

We begin with a general description of the model in Section 2.1. A detailed description requires knowledge of the two-well states; thus in Section 2.2 we provide a the details of the two-well states. Finally, in Section 2.3, we provide a detailed look at the superlattice Hamiltonian.

2.1   Superlattice States I: General Description

The Hamiltonian for the exciton envelope function in a type I semiconductor superlattice (SL) with an applied electric field may be written as [39] [40]:

$$H_{SL}\left(\overrightarrow{r}_e, \overrightarrow{r}_h\right) = H'\left(\overrightarrow{r}_e, \overrightarrow{r}_h\right) + U_e\left(z_e\right) + U_h\left(z_h\right) + eF\left(z_e - z_h\right) , \tag{2.1}$$

where $H'\left(\overrightarrow{r}_e, \overrightarrow{r}_h\right)$ contains the kinetic energy and Coulomb interaction terms, $\overrightarrow{r}_e$ $\left(\overrightarrow{r}_h\right)$ is the electron (hole) coordinate, $U_e\left(z_e\right)$ $\left(U_h\left(z_h\right)\right)$ is the superlattice potential for the electron (hole), e is the modulus of the charge on an electron and F is the strength of the applied static field. The expression for H' is

$$H'\left(\overrightarrow{r}_e, \overrightarrow{r}_h, \rho\right) = \frac{P_{x_e}^2 + P_{y_e}^2}{2m_{e\|}^*} + \frac{P_{z_e}^2}{2m_{ez}^*} + \frac{P_{x_h}^2 + P_{y_h}^2}{2m_{h\|}^*} + \frac{P_{z_h}^2}{2m_{hz}^*} - \frac{e^2}{\varepsilon\sqrt{\rho^2 + z^2}} , \tag{2.2}$$

where P_{ξ_σ}, $\xi_\sigma \in \{x_\sigma, y_\sigma, z_\sigma\}$, $\sigma \in \{e, h\}$ is the momentum operator in the ξ-direction for the particle identified by σ. In Eq. (2.2) the variables z_e and z_h are the z-coordinates (*along the superlattice growth axis*) of the electron and hole, respectively, $z \equiv z_e - z_h$, ρ is the in-plane (*transverse to the growth axis*) electron-hole separation and x_σ, y_σ $\sigma \in \{e, h\}$ are the in-plane position variables. The along-axis and in-plane effective masses of the electron (hole) are denoted m_{ez}^* $\left(m_{hz}^*\right)$ and $m_{e\|}^*$ $\left(m_{h\|}^*\right)$ respectively. The layer dependence of the effective masses is taken into consideration implicitly in Eq. (2.2). To complete the description, ε is the average dielectric constant of the heterostructure.

Defining the in-plane centre of mass coordinate $\overrightarrow{R}_\|$ as

$$\overrightarrow{R}_\| \equiv \frac{m_{e\|}^* \overrightarrow{\rho}_e + m_{h\|}^* \overrightarrow{\rho}_h}{m_{e\|}^* + m_{h\|}^*} , \tag{2.3}$$

14

yields the relationships

$$\vec{\rho}_e = \vec{R}_\parallel - \frac{m_h^*}{m_e^* + m_h^*} \vec{\rho} , \tag{2.4}$$

$$\vec{\rho}_h = \vec{R}_\parallel + \frac{m_e^*}{m_e^* + m_h^*} \vec{\rho} . \tag{2.5}$$

With this change of variables, $H'\left(\vec{r}_e, \vec{r}_h\right)$ becomes

$$H'\left(\vec{r}_e, \vec{r}_h\right) = \frac{P_\parallel^2}{2\left(m_{e\parallel}^* + m_{h\parallel}^*\right)} + \frac{p_\parallel^2}{2\mu} + \frac{p_{z_e}^2}{2m_{ez}^*} + \frac{p_{z_h}^2}{2m_{hz}^*} - \frac{e^2}{\varepsilon\sqrt{\rho^2 + z^2}} , \tag{2.6}$$

where p_{z_e} (p_{z_h}) is the momentum operator in the z-direction for the electron (hole), $P_\parallel$ is the momentum operator for the in-plane centre-of-mass motion and $p_\parallel$ is the momentum operator for the in-plane relative motion. The in-plane electron-hole reduced mass μ is described in terms of the in-plane electron $(m_{e\parallel}^*)$ and hole $(m_{h\parallel}^*)$ effective masses through the relation $\mu^{-1} = \left(m_{e\parallel}^*\right)^{-1} + \left(m_{h\parallel}^*\right)^{-1}$.

It is clear that Eq. (2.1) is independent of the in-plane centre of mass coordinate $\vec{R}_\parallel$, hence the wavefunction defined by the equation $H_{SL}\left|\Psi\right\rangle = E\left|\Psi\right\rangle$ is factorizable such that

$$\psi\left(\vec{r}, \vec{R}\right) = \tilde{N} e^{i\vec{K}\bullet\vec{R}_\parallel} \Psi\left(z_e, z_h, \rho\right) , \tag{2.7}$$

where $\tilde{N}$ is a normalization constant. As we shall see, the factor $\tilde{N} e^{i\vec{K}\bullet\vec{R}_\parallel}$ is unimportant for optically excited states. Thus, from here on we assume that the kinetic energy of the in-plane centre-of-mass is implicitly understood and write $H'\left(\vec{r}_e, \vec{r}_h\right) \Rightarrow H'\left(z_e, z_h, \rho\right)$ where

$$H'\left(z_e, z_h, \rho\right) = \frac{-\hbar^2}{2\mu}\frac{1}{\rho}\frac{\partial}{\partial\rho}\left(\rho\frac{\partial}{\partial\rho}\right) - \frac{\hbar^2}{2}\left[\frac{\partial^2}{\partial z_e m_{ez}^* \partial z_e} + \frac{\partial^2}{\partial z_h m_{hz}^* \partial z_h}\right] - \frac{e^2}{\varepsilon\sqrt{\rho^2 + z^2}} , \tag{2.8}$$

and take $H_{SL}\left|\psi\right\rangle = E\left|\psi\right\rangle$.

Returning to the full Hamiltonian of Eq. (2.1), the superlattice potential $U_\sigma\left(z_\sigma\right), \sigma \in \{e, h\}$ is described by

$$U_\sigma\left(z_\sigma\right) = V_\sigma\left[1 - \sum_j R\left(L_w : z_\sigma - jd\right)\right] , \tag{2.9}$$

15

where d is the superlattice period, V_σ is the well depth, and j is an integer. The function $R(L_w : z)$ is a rectangle function of height 1 and width L_w , the width of the quantum wells.

The exciton Hamiltonian is invariant under a translation of the exciton centre of mass by a distance md, where m is an integer [39][40] . This is because the electric field term in the Hamiltonian depends only on the separation between the electron and the hole and this separation is preserved under such a translation. Translation invariance allows the exciton envelope function to be written in the form

$$\psi_\mu^q (z_e, z_h, \rho) = \frac{1}{\sqrt{2N+1}} \sum_m e^{iqmd} W_\mu (z_e - md, z_h - md, \rho) \ , \qquad (2.10)$$

where μ is the superlattice exciton quantum number of internal motion, q is the exciton centre-of-mass wavenumber in the z-direction, $2N+1$ is the number of periods in the superlattice and $W_\mu (z_e, z_h, \rho)$ is an exciton Wannier function.

In much the same way as Dignam & Sipe [39][40], we expand the Wannier functions in a tight-binding calculation over the eigenstates, $\left| \phi_j^\beta \right\rangle$, of the electric field independent two-well Hamiltonians

$$H_j^{TW} (z_e, z_h, \rho) = \widetilde{H}_{TW} (z_e, z_h, \rho) + V_e (1 - R_e (L_w; z_e - jd)) + V_h (1 - R(L_w; z_h)) \ , \qquad (2.11)$$

where $\widetilde{H}_{TW} (z_e, z_h, \rho)$ are the kinetic energy and Coulomb contributions, and $V_\sigma (1 - R_\sigma (L_w; z_\sigma - jd))$ $\{\sigma = e, h\}$ are the well potentials seen by the electron and hole. Explicitly, H_j^{TW} is the Hamiltonian for an exciton where the electron (hole) potential consists of a quantum well centered at $z = jd$ ($z = 0$). In this work we consider both bound and continuum eigenstates of the two-well Hamiltonians as a basis for the Wannier functions. The model presented therefore goes well beyond the work by Dignam & Sipe which only considered 1S states. The two-well problem is discussed in detail in the next subsection.

The eigenstates of the superlattice Hamiltonian Eq. (2.1), as a tight binding of the two-well states of all possible electron-hole separations, j, centered on all possible sites, m, can be

16

written

$$|\psi_\mu^q\rangle = \frac{1}{\sqrt{2N+1}} \sum_{m=-N}^{N} \sum_{j=-N}^{N} \sum_{\beta=1}^{M} e^{iqmd} B_{j,\beta}^\mu \left|\Phi_j^\beta(m)\right\rangle , \qquad (2.12)$$

where β is the two-well eigenstate quantum number and

$$\left\langle z_e, z_h, \rho \,\middle|\, \Phi_j^\beta(m)\right\rangle \equiv \Phi_j^\beta(z_e, z_h, \rho) . \qquad (2.13)$$

Comparing Eq. (2.12) with Eq. (2.10) and using Eq. (2.13) we see that the Wannier functions can be written

$$W_\mu(z_e, z_h, \rho) = \sum_{j=-N}^{N} \sum_{\beta=1}^{M} B_{j,\beta}^\mu \Phi_j^\beta(z_e - jd, z_h, \rho) . \qquad (2.14)$$

A complete discussion of the determination of the two-well eigenstates follows in the section titled Two-Well States.

The form of the superlattice wavefunction given in Eq. (2.12) allows the field-dependent excitonic absorption per unit volume, $\alpha(\omega)$, to be written as [40]

$$\alpha(\omega) = \sum_\mu \frac{4\pi e^2 \left|\widehat{\xi} \cdot \vec{p}_{cv}\right|^2}{\omega m_0^2 \eta(\omega) c} \alpha_\mu \delta(E_\mu(q) - \hbar\omega) , \qquad (2.15)$$

where $\widehat{\xi}$ is the electric field polarization vector, $\vec{p}_{cv}$ is the momentum matrix element between the bulk conduction band and valence band Bloch states at the band edges, m_0 is the free electron mass, $\eta(\omega)$ is the frequency dependent refractive index of the medium, and the absorption strength, α_μ, is given by

$$\alpha_\mu = \delta_{q,0} \frac{1}{d} \left|\int dz W^\mu(\rho = 0, z, z)\right|^2 . \qquad (2.16)$$

The form for the frequency dependent absorption given in Eq.(2.15) cannot be used in a compu-

17

tation because of the delta function. It can however be well approximated using a Lorentzian.

$$\alpha(\omega) = \sum_{\mu} \frac{4\pi e^2 \left|\hat{\xi} \cdot \overrightarrow{P}_{cv}\right|^2}{\omega m_0^2 \eta(\omega) c} \alpha_\mu \delta\left(E_\mu(q) - \hbar\omega\right) \tag{2.17a}$$

$$\simeq A \sum_{\mu} \alpha_\mu \delta\left(E_\mu(q) - \hbar\omega\right) \tag{2.17b}$$

$$\simeq A \sum_{\mu} \alpha_\mu \frac{\left(\dfrac{\Delta E}{2\pi}\right)}{(E - \hbar\omega)^2 + \left(\dfrac{\Delta E}{2}\right)^2} \tag{2.17c}$$

where A is a constant and ΔE is the FWHM of each line. This linewidth is associated with the scattering times of the excitonic states and is typically $\lesssim 2$ meV for a temperature of $T = 10$ K. In moving from Eq. (2.17a) to Eq. (2.17b) we have assumed that the refractive index is constant for the frequency range of interest. Also, since we will be looking at the absorption spectrum over a range of roughly 0.05 eV where $\hbar\omega \approx 1.5eV$, the fractional change in ω is about 3%. This is on the order of other approximations made in arriving at Eq. (2.15) thus we neglect this variation. The absorption spectra graphs in the following chapter are based on Eq. (2.17c), and show $\dfrac{\alpha(\omega)}{A}$.

It is clear from Eq. (2.16) that the absorption differs from zero only if the exciton wave number, q, in the z-direction is zero . Thus in what follows the superscript q is dropped and the exciton wavenumber in the z-direction is assumed to be zero. Also the dependence of the wavefunction on the superlattice quantum number μ will be indicated using a superscript instead of the previously used subscript. That is we write

$$\left|\psi_\mu^0\right\rangle \equiv \left|\psi^\mu\right\rangle \tag{2.18a}$$

$$= \frac{1}{\sqrt{2N+1}} \sum_{m=-N}^{N} \sum_{j=-N}^{N} \sum_{\beta=1}^{M} B_{j,\beta}^\mu \left|\Phi_j^\beta(m)\right\rangle . \tag{2.18b}$$

Using this wavefunction, the time-independent Schrödinger equation for the superlattice can be stated

$$H_{SL} \left|\psi^\mu\right\rangle = E^\mu \left|\psi^\mu\right\rangle . \tag{2.19}$$

18

Thus we obtain

$$\langle \psi^\nu | H_{SL} | \psi^\mu \rangle = E^\mu \langle \psi^\nu | \psi^\mu \rangle \ . \tag{2.20}$$

Then, inserting Eq. (2.18b) into Eq. (2.20) we have

$$\sum_{m,m'} \sum_{i,j} \sum_{\alpha,\beta} B_{i,\alpha}^{\nu*} B_{j,\beta}^{\mu} \left\langle \Phi_i^\alpha (m') | H_{SL} | \Phi_j^\beta (m) \right\rangle = E^\mu \sum_{m,m'} \sum_{i,j} \sum_{\alpha,\beta} B_{i,\alpha}^{\nu*} B_{j,\beta}^{\mu} \left\langle \Phi_i^\alpha (m') | \Phi_j^\beta (m) \right\rangle \ . \tag{2.21}$$

Minimizing this with respect to $B_{j,\beta}^\mu$, we obtain

$$\sum_{m,m'} \left\langle \Phi_i^\alpha (m') | H_{SL} | \Phi_j^\beta (m) \right\rangle B_{j,\beta}^\mu = E^\mu \sum_{m,m'} \left\langle \Phi_i^\alpha (m') | \Phi_j^\beta (m) \right\rangle B_{j,\beta}^\mu \ . \tag{2.22}$$

Thus the problem of determining the eigenvalues of the superlattice Hamiltonian reduces to the solution of the generalized eigenvalue equation

$$H_{ij}^{\alpha\beta} B_{j,\beta}^\mu = E^\mu O_{ij}^{\alpha\beta} B_{j,\beta}^\mu \ , \tag{2.23}$$

where $O_{ij}^{\alpha\beta} \equiv \sum_{m,m'} \left\langle \Phi_i^\alpha (m') | \Phi_j^\beta (m) \right\rangle$ is an "overlap matrix" element. The "overlap matrix" arises because we are using a non-orthogonal basis in our expansion. We now turn to the problem of determining the electric field independent two-well eigenstates before continuing with the details of the SL Hamiltonian.

2.2 Two-Well States

As noted above, the Wannier functions used in the expansion for the eigenstates of the super-lattice Hamiltonian Eq. (2.1) are created by a tight-binding of the eigenstates of the two-well (TW) Hamiltonians given in Eq. (2.11). Each of these Hamiltonians is characterized by an integer index j that gives the separation of the electron and hole, i.e. the distance between the wells is jd where d is the period of the superlattice of interest.

19

In the two mini-band approximation, a two-well Hamiltonian, $H_j^{TW}(z_e, z_h, \vec{\rho})$ may be written as

$$H_j^{TW}(z_e, z_h, \vec{\rho}) = T + V(|\vec{r}_e - \vec{r}_h|) + V_e[1 - R(L; z_e - jd)] + V_h[1 - R(L_w; z_h)]. \quad (2.24)$$

Here the well depths $V_{e,h}$ and the rectangle functions $R(L_w; z_{e,h})$ are the same as those in the description of Eq. (2.8) and Eq. (2.9) above. In Figure 2-1 we sketch a schematic of the potential profiles for the electron and hole in a two-well state.
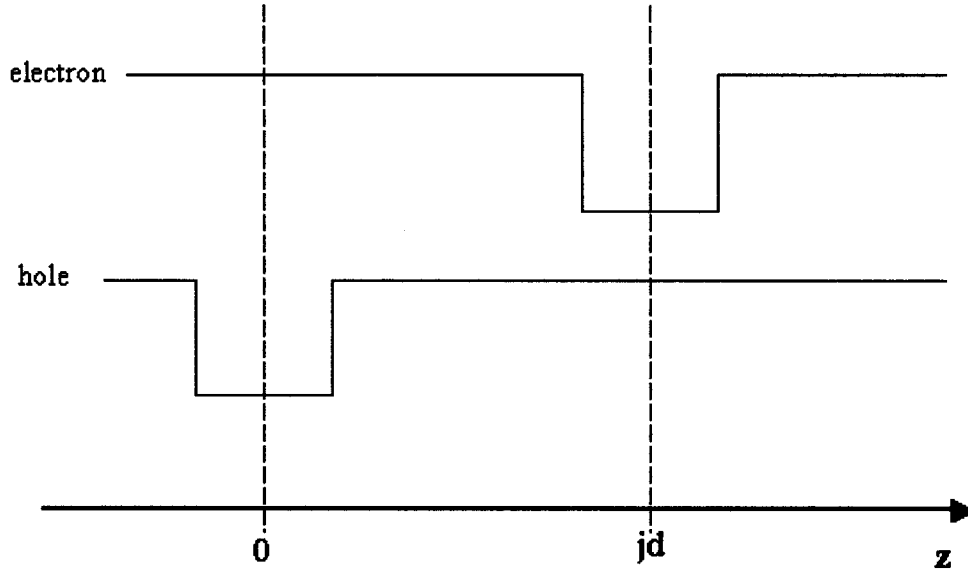
Figure 2-1: Potential profile for a two-well state where the electron and hole are separated by a distance jd.

In order to simplify the discussion in the following treatment, we consider, for the moment, only the kinetic and Coulomb energy part of the two-well Hamiltonian. To this effect, we define the kinetic energy and Coulomb interaction portion of a two-well Hamiltonian for a fixed well separation jd

$$\widetilde{H}_{TW} \equiv H_j^{TW}(z_e, z_h, \vec{\rho}) - (V_e[1 - R(L; z_e - jd)] + V_h[1 - R(L; z_h)]) \quad (2.25a)$$

$$= T + V(|\vec{r}_e - \vec{r}_h|) \quad (2.25b)$$

20

Only excitons with s-symmetry can be optically created [46]. Thus we choose for our basis only radially symmetric two-well states. The s-like eigenstates of $\tilde{H}_{TW}$ are radially symmetric. Under the assumptions stated above and using a cylindrical coordinate system where z represents the growth axis, the kinetic energy and Coulomb interaction portions of the TW Hamiltonian can be written

$$\tilde{H}_{TW}\left(z_e, z_h, \vec{\rho}\right) = \frac{-\hbar^2}{2\mu}\left(\frac{1}{\rho}\frac{\partial}{\partial\rho}\left(\rho\frac{\partial}{\partial\rho}\right) + \frac{1}{\rho^2}\frac{\partial^2}{\partial\theta^2}\right) - \frac{\hbar^2}{2}\frac{\partial}{\partial z_e}\frac{1}{m_{ez}^*}\frac{\partial}{\partial z_e} - \frac{\hbar^2}{2}\frac{\partial}{\partial z_h}\frac{1}{m_{hz}^*}\frac{\partial}{\partial z_h} - \frac{e^2}{\varepsilon\sqrt{\rho^2 + z^2}} \ .$$

(2.26)

Finally, since states with s-symmetry have no explicit angular dependence, Eq.(2.26) reduces to

$$\tilde{H}_{TW}\left(z_e, z_h, \rho\right) = \frac{-\hbar^2}{2\mu}\frac{1}{\rho}\frac{\partial}{\partial\rho}\left(\rho\frac{\partial}{\partial\rho}\right) - \frac{\hbar^2}{2}\left(\frac{\partial}{\partial z_e}\frac{1}{m_{ez}^*}\frac{\partial}{\partial z_e} + \frac{\partial}{\partial z_h}\frac{1}{m_{hz}^*}\frac{\partial}{\partial z_h}\right) - \frac{e^2}{\varepsilon\sqrt{\rho^2 + z^2}} \ .$$

(2.27)

Returning to the full TW Hamiltonian, we consider solutions to the equation

$$H_j^{TW}\left|\psi\right\rangle = E_j\left|\psi\right\rangle \ ,$$

(2.28)

for a fixed electron/hole separation jd . In order to simplify the notation in what follows we assume that the fixed separation identifier j is understood and define $H^{TW} \equiv H_j^{TW}$. To solve equation (2.28) we expand the TW eigenstates in terms of a set of orthonormal basis states, $\left|\phi_k\right\rangle$. We write the basis functions $\phi_k\left(z_e, z_h, \rho\right)$:

$$\left|\Phi_j^\beta\left(0\right)\right\rangle = \sum_k A_k^{j,\beta}\left|\phi_k\right\rangle \ .$$

We write the basis functions $\phi_k\left(z_e, z_h, \rho\right)$ as

$$\phi_k\left(z_e, z_h, \rho\right) = f_e\left(z_e\right) f_h\left(z_h\right) g_k\left(\rho\right) \ ,$$

(2.29)

where $f_\sigma\left(z_\sigma\right)$, $\sigma \in \{e, h\}$ are envelope functions in the z-direction, and $g_k\left(\rho\right)$ is the kth in-plane basis function (as yet to be specified). We note that factorizing ϕ_k into a product of z_e, z_h, and

21

ρ dependent functions is an approximation. In general, the exciton is 3-dimensional. However, it has been shown [40] that this is a good approximation as long as the well width is not too large $\left(L_W \lesssim 100 \text{ Å}\right)$. Because our full superlattice wavefunction consists of a sum of ϕ_k , it does contain the z-dependence of the electron-hole correlations, which is essential to a proper description of a superlattice exciton.

The envelope functions along the growth axis are the single particle eigenstates of a finite quantum well and are defined as

$$
f_\sigma\left(z_\sigma\right) = \begin{cases} A_\sigma e^{\gamma_\sigma z_\sigma} & \text{if} \quad z_\sigma < \frac{-L}{2} \\ B_\sigma \cos\left(\kappa_\sigma z_\sigma\right) & \text{if} \quad |z_\sigma| \le \frac{L}{2} \\ C_\sigma e^{-\tau_\sigma z_\sigma} & \text{if} \quad z_\sigma > \frac{L}{2} \end{cases} , \tag{2.30}
$$

where the coefficients A, B, and C are determined by requiring that $\phi_k\left(z_e, z_h, \rho\right)$ is normalized and continuous at the layer interfaces. The parameters γ_σ and τ_σ are determined via the continuity of the derivative of $f_\sigma\left(z_\sigma\right)$ at the layer interfaces and κ_σ is determined using the quantization condition in the usual way [43] .

With the additional assumption that $g_k\left(\rho\right)$ also varies slowly over a unit cell, the Coulomb contribution, $V_{k,k'}$ to a two-well Hamiltonian matrix element can be written

$$
\begin{aligned}
V_{k,k'} &= \langle\phi_k|\, V\,|\phi_{k'}\rangle && (2.31) \\
&= \int_{-\infty}^{\infty} dz_e\, f_e^{\,2}\left(z_e\right) \int_{-\infty}^{\infty} dz_h\, f_h^{\,2}\left(z_h\right) \int_0^R d\rho\rho g_k\left(\rho\right) g_{k'}\left(\rho\right)\left(\frac{-e^2}{\varepsilon\sqrt{\rho^2+z^2}}\right) , && (2.32)
\end{aligned}
$$

where R corresponds to the maximum in-plane electron-hole separation that we wish to consider. Strictly speaking, R should be infinite, however, as we discuss shortly, we choose a finite R to allow the calculation of a discrete (as opposed to continuous) basis set. In practice we work in units of the exciton Bohr radius $a_0 \equiv \dfrac{\hbar^2 \varepsilon}{\mu\, e^2}$ (for GaAs is $a_0 \simeq 157\text{Å}$) and find that a choice of $R = 30a_0$ provides an in-plane radius large enough to cover the band yet small enough to yield higher energy quasi-continuum states.

The key problem now is to determine the in-plane basis states $g_k\left(\rho\right)$. One possible choice for an in-plane basis would be the exact wavefunctions for a 2D bulk exciton which are given in terms of the associated Laguerre polynomials[42]. These however lead to computational

22

difficulties when evaluating the Coulombic contribution to the matrix elements of the two-well Hamiltonian. We opt instead to use Bessel functions of the first kind of order 0, that is

$$g_k(\rho) \equiv N_k J_0(k\rho) \ ,$$

(2.33)

where N_k is a normalization constant given by

$$N_k = \frac{\sqrt{2}}{R \ |J_1(kR)|}$$

The wavenumber k is determined from the solution of

$$\frac{-\hbar^2}{2\mu} \frac{1}{\rho} \frac{\partial}{\partial \rho} \left(\rho \frac{\partial}{\partial \rho} \right) g(\rho) - Eg(\rho) = 0$$

(2.34)

where $\rho \in (0, R)$, $g(R) = 0$, and $k^2 = \frac{2\mu E}{\hbar^2}$. Thus the $g_k(\rho)$, are the eigenstates of the finite system $(R \neq \infty)$ in the absence of the Coulomb interaction.

One key advantage of this basis is that both the kinetic energy and the Coulomb matrix elements are relatively easy to evaluate when compared to a plane-wave basis. Comparing a 2D bulk calculation using a Bessel function basis with the exact results given in reference [42] we find good agreement in both the energies and wavefunctions at $R = 30a_0$ for first 3 bound states using a 300 k-state basis.

In Figure 2-2 through Figure 2-4 we show a comparison of the exact 2D bulk wavefunctions from reference [42] with wavefunctions determined by our model for an in-plane radius of $R = 30a_0$ calculated using 300 k-states. The material parameters listed in Table 2.1 below were used for these and all other calculations presented in this thesis. We note that though the barrier masses are included in that table, they are not used in the pure 2D calculation.

23

Parameter	GaAs/Ga$_{0.7}$Al$_{0.3}$As
m^*_{ez} (well)	0.0665
$m^*_{e\parallel}$ (well)	0.0665
m^*_{hz} (well)	0.34
$m^*_{h\parallel}$ (well)	0.115
m^*_{ez} (barrier)	0.08
$m^*_{e\parallel}$ (barrier)	0.08
m^*_{hz} (barrier)	0.45
$m^*_{h\parallel}$ (barrier)	0.165
ε	12.5
V_e	318 meV
V_h	164 meV
E_{gap} (GaAs)	1510.7 meV

Table 2.1: The material parameters used for all calculations presented in this thesis are those used by Dignam & Sipe (Ref. [39]). The particle effective masses are all given in terms of the free electron mass.
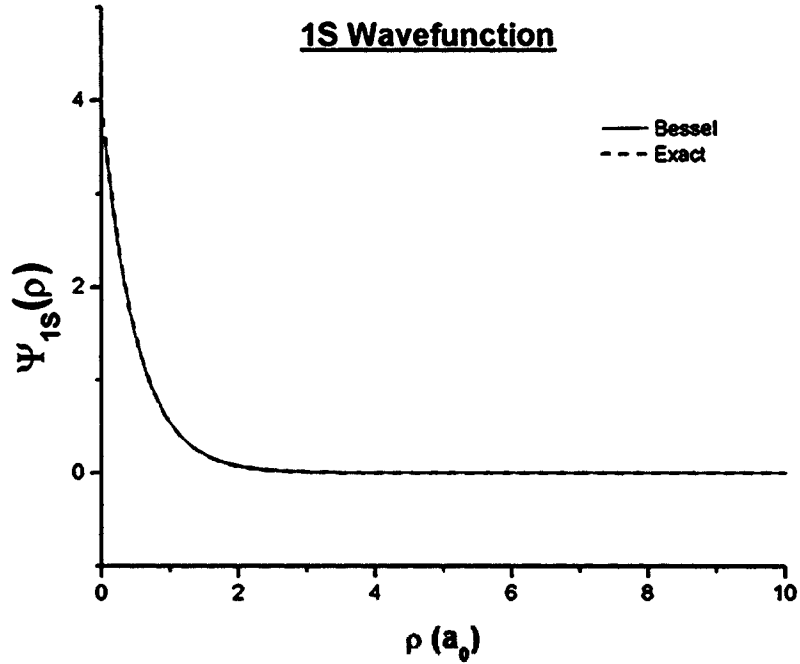
Figure 2-2: Bessel function expansion 1S wavefunction determined using $R = 30a_0$ and 300 k-states vs. the exact wavefunction.

24
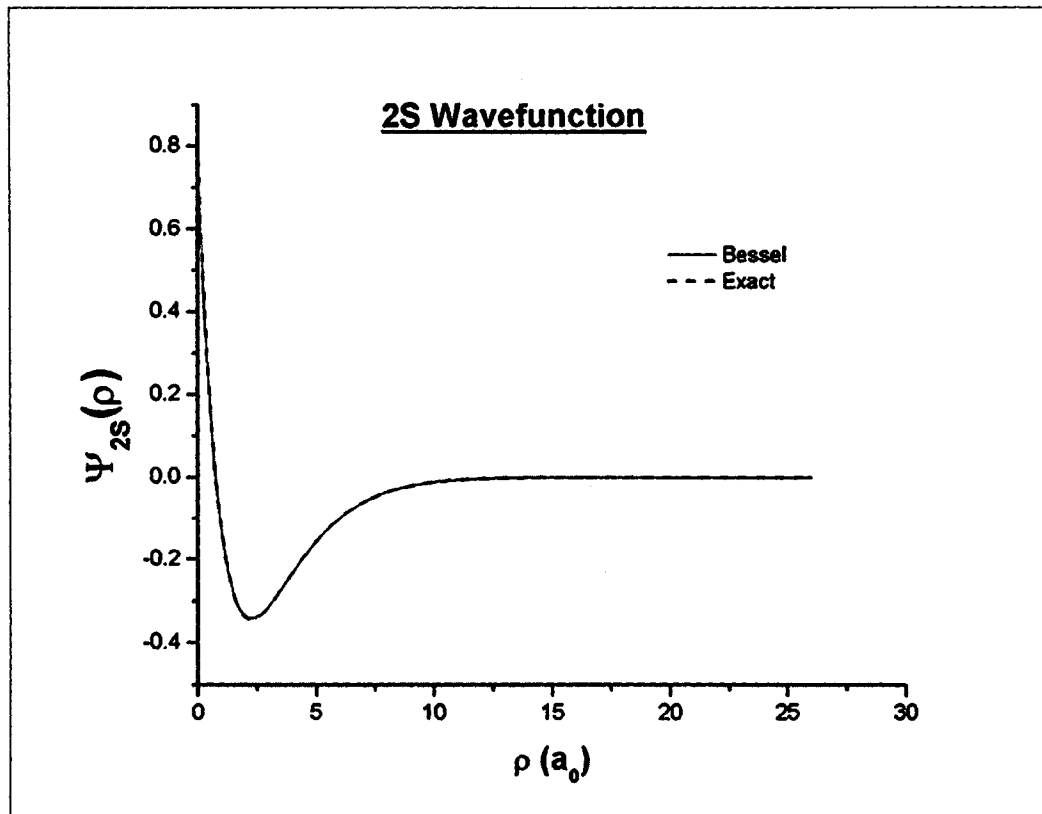
2S Wavefunction

Figure 2-3: Comparison of the exact 2S wavefunction with the wavefunction determined from the Bessel function expansion.

25
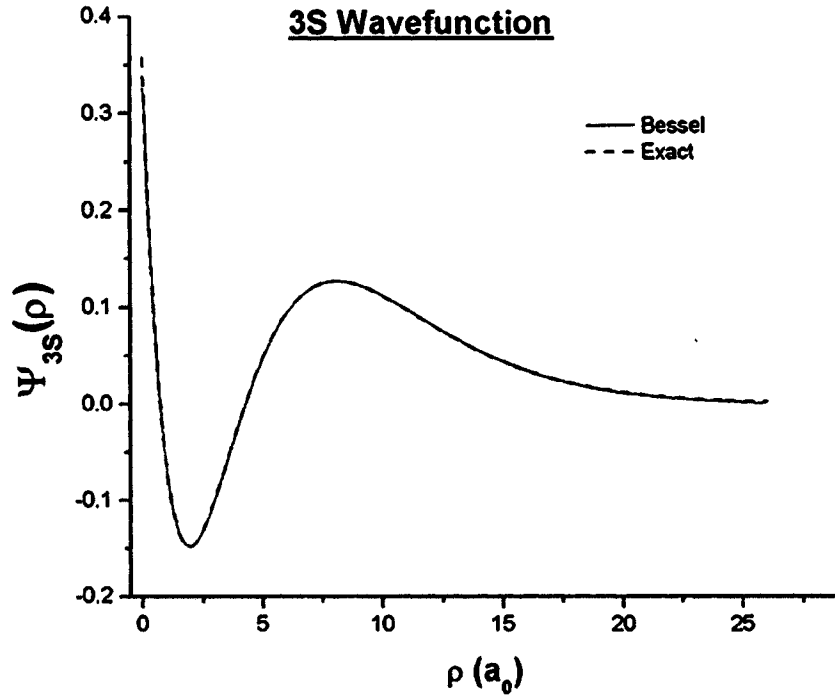
3S Wavefunction

Figure 2-4: 3S Wavefunction.

We can resolve 5 bound states using 300 k-states at $R = 30a_0$. Though we get very good agreement with the analytical wavefunctions up to the 3S state, our model does not provide accurate results for the 4S and 5S wavefunctions. Figure 2-5 shows the match between our 4S wavefunction and the exact. We see that though our wavefunction preserves the general trend of the exact wavefunction, it is not very accurate. This is not of critical importance because the oscillator strengths associated with these high-lying bound states is very small.

26
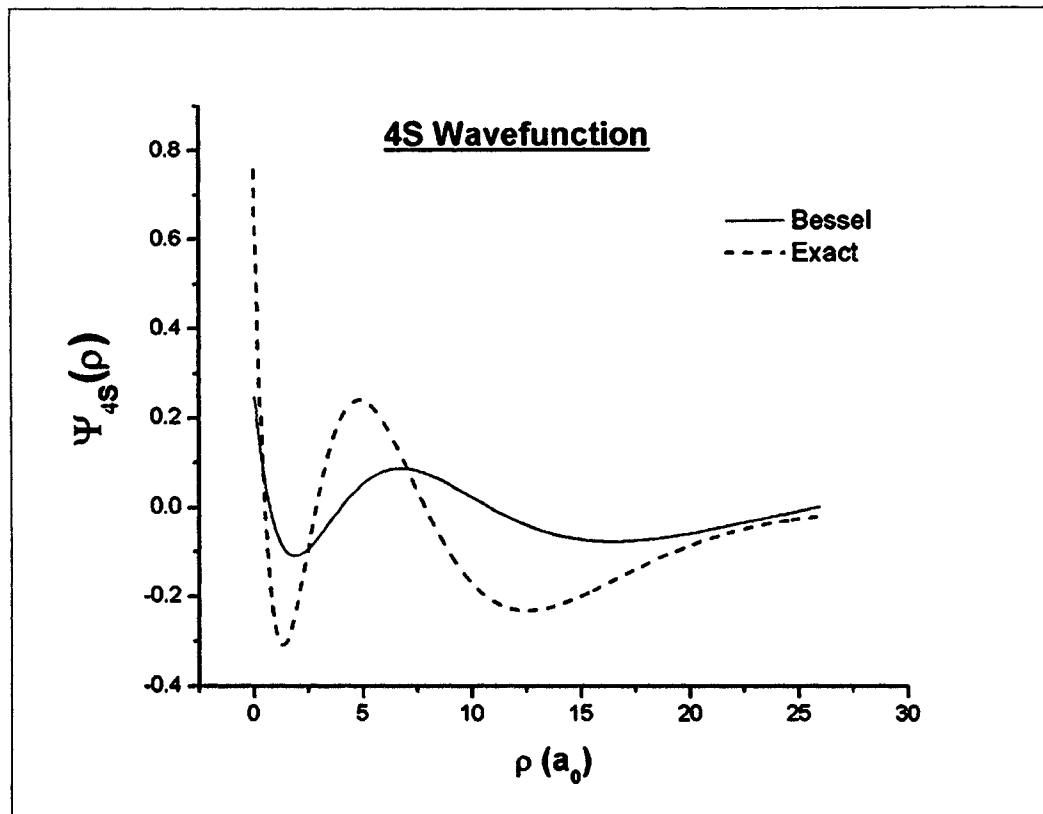
4S Wavefunction

Figure 2-5: The Bessel expansion wavefunction for the 4S state preserves the general trend of the exact wavefunction but the agreement is not very accurate.

The value of R and the number of k-states to use in our TW model has been carefully selected. For example, for $R = 10a_o$, even with the computationally intensive inclusion of 1000 k-states, the results do not provide an accurate match to the exact excitonic bound states for a purely 2D system. After extensive testing at a variety of R values, we found, as stated in the previous paragraph, that a radial extent of $R = 30a_o$ with the inclusion of 300 k-states provided the necessary accuracy while remaining computationally tractable. These parameters generate TW states that, when used in the SL model, provide SL absorption spectra in excellent agreement with experimental results at lower photon energies over a wide range of static field strengths using a Lorentzian FWHM comparable to the FWHM of the experimental determinations. However, at higher photon energies, the calculated absorption spectra suffer from oscillations in the absorption lineshape. The oscillations can be eliminated by increasing the Lorentzian bandwidth (see Eq. (2.17a)), though doing so degrades the overall match to

27

experimental results. The source of these oscillations can be attributed to the increasing energy separations between TW states as their energies increase. Thus we are presented with the further requirement of having an energy spacing between the basis states, over the range of interest, with separations comparable to, or less than, the peak FWHM from experimental results (~1.5-2.0 meV [49]). We found that TW states generated using 500 k-states at $R = 40a_0$ should provide the necessary fineness in the energy grid along with satisfying our other requirements. A comparison, in table form, between the energies of the bound TW states determined for the electron and hole in the same well (0 separation in z), for $R = 30a_0$ (300 k-states) and $R = 40a_0$ (400 k=states), is shown in Appendix A. Also included in Appendix A are graphs and further discussion in support of the arguments presented here concerning the choice of radial extent and the number of included k-states. The price one pays for increasing R is an increase in the computation time. Thus for the superlattice calculation we use the TW states determined using $R = 30a_0$ and 300 k-states.

We further test our TW model by calculating the absorption spectrum for a single well in the absence of Coulomb interaction and without an applied field. Inserting the explicit form for the Wannier functions into Eq. (2.16) we get the following expression for the absorption strengths.

$$\alpha_\mu = \frac{1}{d} \left| \sum_{n,\beta} B^\mu_{n,\beta} \sum_k N_k \, A^{n,\beta}_k \int dz f_e\left(z - nd\right) f_h\left(z\right) \right|^2 . \tag{2.35}$$

This simple form for the absorption strength arises because $J_0\left(0\right) = 1$.

The TW zero-field, single-well spectrum for non-interacting electrons and holes is well known to be a step function rising at the band edge. We find that our model provides excellent agreement with this result as shown in Figure 2-6. The absorption spectrum shown in Figure 2-6 was calculated using Eq. (2.17a) and using 50, $R = 30a_0$, TW eigenfunctions with an initial Lorentzian FWHM of 0.1 meV at a photon energy of 1550 meV to a maximum FWHM of 3.5 meV at a photon energy of 1800 meV. The adaptive (linear) bandwidth was used to smooth out *oscillations* in the lineshape that arose due to increasing separations between TW eigen-energies. The *oscillations* can still be seen between approximately 1640 meV and 1650 meV and again between 1675 meV and 1700 meV. Spectra without the variable FWHM ΔE

28

are shown in Appendix A.
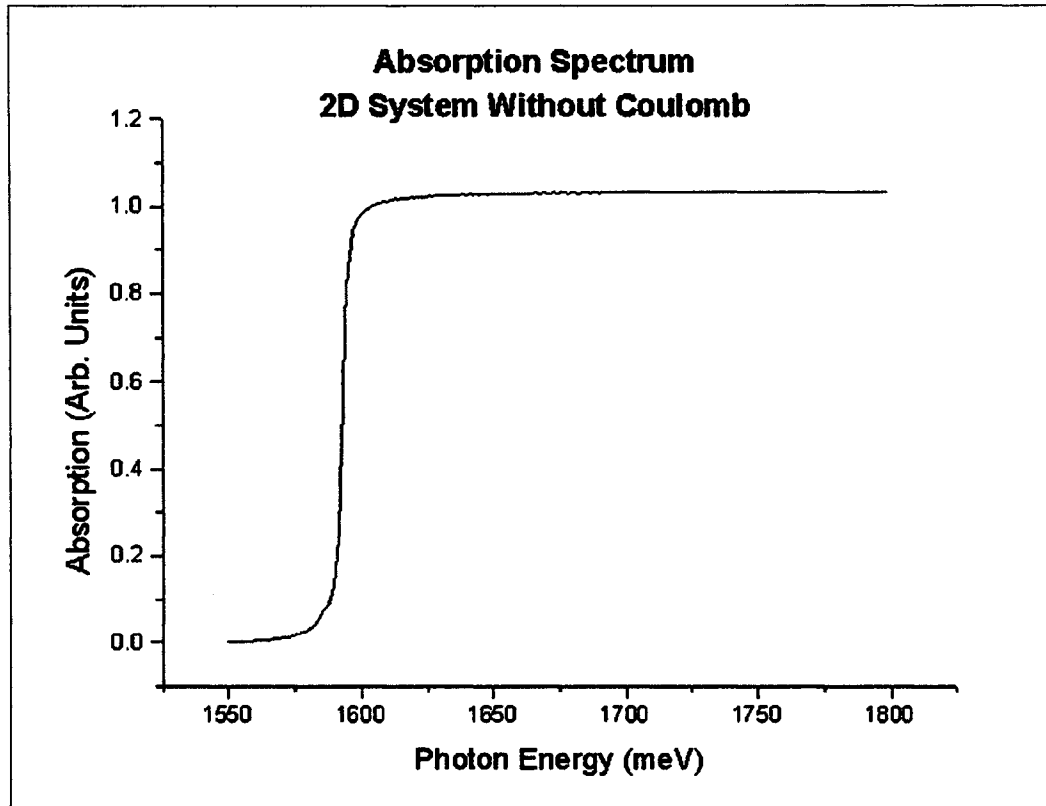
Figure 2-6: Absorption spectrum for a purely 2D system in the absence of Coulomb interaction and no applied field.

Having demonstrated the accuracy of our basis, we return to the problem of implementing it for the full TW exciton problem.

The main source of the computational efficiency provided by this basis stems from ease with which the Coulomb matrix elements can be evaluated. From Eq. (2.31) we see that

$$V_{k,k'} \propto \int_0^R d\rho\, \rho J_0\left(k\rho\right) J_0\left(k'\rho\right) \frac{1}{\sqrt{\rho^2 + z^2}} \, . \tag{2.36}$$

Using the following integral representation [45]

$$\frac{1}{\sqrt{\rho^2 + z^2}} = \frac{2}{\pi} \int_0^\infty d\alpha \cos\left(\alpha z\right) K_0\left(\alpha \rho\right) \, . \tag{2.37}$$

29

gives

$$V_{k,k'} = N_k N_{k'} \int_0^\infty d\alpha \int \int dz_e dz_h f_e{}^2 (z_e) \ f_h{}^2 (z_h) \cos(\alpha [z_e - z_h]) \int_0^R d\rho \rho J_0 (k\rho) J_0 (k'\rho) K_0 (\alpha\rho) \ .$$

(2.38)

The integrals over z_σ are analytic and thus pose no difficulty to a computational solution. There is, however, no closed-form solution to the integral over ρ . This proves to be a limiting factor affecting computational efficiency. A large improvement to computational speed can be achieved using the approximation

$$\int_0^R d\rho \rho J_0 (k\rho) J_0 (k'\rho) K_0 (\alpha\rho) \ \simeq \ \int_0^\infty d\rho \rho J_0 (k\rho) J_0 (k'\rho) K_0 (\alpha\rho)$$

(2.39)

$$= \ \left(k^4 + \alpha^4 + k'^4 - 2k^2 k'^2 + 2k^2 \alpha^2 + 2\alpha^2 k'^2 \right)^{-\frac{1}{2}} \ .$$

If we index the in-plane wavenumbers, k, against integers i with the ground state corresponding to $i = 0$ and excited states following incrementally, we find that for wavenumbers k_i and k_j where $|i - j| > 30$, the approximation Eq. (2.39) provides results with acceptable accuracy. However, for $|i - j| \le 30$, the approximation does not provide accurate results and the integral in Eq. (2.38) must be solved numerically.

Now that we have determined the explicit form for the TW states, we are in a position to discuss the details of the SL Hamiltonian.

2.3 Superlattice States II: Details of the Hamiltonian

The eigenstates of our TW Hamiltonian are not exact. However, in order to proceed with the solution for the SL problem we make the assumption that the TW wavefunctions and energies determined above are exact. This has been shown to be a good approximation by Dignam & Sipe [39][40] .

30

The SL wavefunctions can now be written

$$\psi^\mu(z_e, z_h, \rho) = \frac{1}{\sqrt{2N+1}} \sum_{m=-N}^{N} \sum_{j=-N}^{N} \sum_{\beta=1}^{M} B_{j,\beta}^\mu \quad f_e(z_e - (j+m)d) \quad f_h(z_h - md) \sum_k N_k A_k^{j,\beta} J_0(k\rho) \ .$$

$$(2.40)$$

In arriving at this explicit form of the SL wavefunctions we have chosen an expansion of the Wannier functions in terms of the TW eigenstates with the hole centered at $z_h = 0$. As has been shown by Dignam & Sipe [40] , the results are independent of the choice of origin.

Comparing Eq.(2.23) and Eq.(2.22) we see that a typical Hamiltonian matrix element is given by

$$H_{ij}^{\alpha\beta} = \sum_{m,m'} \left\langle \Phi_i^\alpha(m') \,|H_{SL}|\Phi_j^\beta(m) \right\rangle \ .$$

$$(2.41)$$

Inserting closure we can write

$$H_{ij}^{\alpha\beta} = \sum_{m,m'} \int dz_e \, dz_h \, \rho d\rho \, \Phi_i^{*\alpha}(z_e - md, z_h - md, \rho) H_{SL}(z_e, z_h, \rho) \, \Phi_j^\beta(z_e - m'd, z_h - m'd, \rho) \ .$$

$$(2.42)$$

Taking advantage of the translational invariance of the SL Hamiltonian, we make a change of variables and set $z'_\sigma = z_\sigma - m'd$; $\sigma = e, h$ to get

$$H_{ij}^{\alpha\beta} = \sum_{m} \int dz_e \, dz_h \, \rho d\rho \, \Phi_i^{*\alpha}(z_e - md, z_h - md, \rho) H_{SL}(z_e, z_h, \rho) \, \Phi_j^\beta(z_e, z_h, \rho) \ , \quad (2.43)$$

which gives

$$H_{ij}^{\alpha\beta} = \sum_{m} \left\langle \Phi_i^\alpha(m) \,|H_{SL}|\Phi_j^\beta(0) \right\rangle \ .$$

$$(2.44)$$

Similarly,

$$O_{ij}^{\alpha\beta} = \sum_{m} \left\langle \Phi_i^\alpha(m) \mid \Phi_j^\beta(0) \right\rangle \ .$$

$$(2.45)$$

31

These forms for the necessary matrix elements prove to be computationally convenient.

To simplify the calculation of the SL Hamiltonian matrix, we write the SL Hamiltonian in terms of the TW Hamiltonian as follows

$$H_{SL}\left(z_e, z_h, \rho\right) = H_j^{TW}\left(z_e, z_h, \rho\right) + \Delta_j\left(z_e, z_h\right) + eF\left(z_e - z_h\right) , \tag{2.46}$$

where the lattice potential is given by

$$\Delta_j\left(z_e, z_h\right) = -V_e \sum_{n \neq j} R\left(L; z_e - nd\right) - V_h \sum_{n \neq 0} R\left(L; z_h - nd\right) . \tag{2.47}$$

Clearly, this form for the lattice potential includes the potentials due to the lattice except for those included in the TW Hamiltonian, namely the electron potential due to the jth well and the hole potential in the 0th well. Using Eq. (2.46) in Eq. (2.44) yields

$$\begin{aligned}
H_{ij}^{\alpha\beta} &= \sum_m \left[\left\langle \Phi_i^\alpha\left(m\right) \mid \Phi_j^\beta\left(0\right) \right\rangle E_{j,\beta}^{TW} + \left\langle \Phi_i^\alpha\left(m\right) \left| \Delta_j\left(z_e, z_h\right) \right| \Phi_j^\beta\left(0\right) \right\rangle \right. \\
&\quad \left. + eF \left\{ \left\langle \Phi_i^\alpha\left(m\right) \mid z_e \mid \Phi_j^\beta\left(0\right) \right\rangle - \left\langle \Phi_i^\alpha\left(m\right) \mid z_h \mid \Phi_j^\beta\left(0\right) \right\rangle \right\} \right] ,
\end{aligned} \tag{2.48}$$

where $E_{j,\beta}^{TW}$ is the TW energy eigenvalue corresponding to the βS state for an exciton where the electron and hole are separated by j periods of the lattice. Here βS can either represent a bound or a continuum state. We insert closure and consider a termwise analysis of Eq. (2.48).

32

The first term arises due to the TW Hamiltonian.

$$H_{ij}^{\alpha\beta}(1) \equiv E_{j,\beta}^{TW} \sum_m \left\langle \Phi_i^\alpha(m) \mid \Phi_j^\beta(0) \right\rangle \tag{2.49a}$$

$$\underset{closure}{=} E_{j,\beta}^{TW} \sum_m \left[\int dz_e f_e(z_e - (i+m)d) f_e(z_e - (j+m)d) \int dz_h f_h(z_h - md) f_h(z_h) \right. \tag{2.49b}$$

$$\left. \times \sum_{k,k'} A_k^{\alpha,i} A_{k'}^{\beta,j} N_k N_{k'} \int \rho d\rho J_0(k\rho) J_0(k'\rho) \right]$$

$$= E_{j\beta}^{TW} \sum_m \left[\int_{-\infty}^\infty dz_e f_e(z_e - (i+m)d) f_e(z_e - jd) \int_{-\infty}^\infty dz_h f_h(z_h - md) f_h(z_h) \right. \tag{2.49c}$$

$$\left. \times \sum_k A_k^{\alpha,i} A_k^{\beta,j} \right] .$$

The final form given in Eq. (2.49a) arises because

$$N_k N_{k'} \int \rho d\rho J_0(k\rho) J_0(k'\rho) = \delta_{k,k'}.$$

A similar analysis gives the explicit forms for the final two terms that make up given matrix element:

$$H_{ij}^{\alpha\beta}(2) \equiv \sum_m \left\langle \Phi_i^\alpha(m) \mid \Delta_j(z_e, z_h) \mid \Phi_j^\beta(0) \right\rangle \tag{2.50a}$$

$$\underset{closure}{=} -\sum_m \sum_k A_k^{\alpha,i} A_k^{\beta,j} V_e \sum_{n \neq j} \left\{ \begin{array}{c} \int_{nd-\frac{L}{2}}^{nd+\frac{L}{2}} dz_e f_e(z_e - (i+m)d) f_e(z_e - jd) \\ \times \int_{-\infty}^\infty dz_h f_h(z_h - md) f_h(z_h) \end{array} \right\} \tag{2.50b}$$

$$+ V_h \sum_{n \neq 0} \left\{ \int_{-\infty}^\infty dz_e f_e(z_e - (i+m)d) f_e(z_e - jd) \int_{nd-\frac{L}{2}}^{nd+\frac{L}{2}} dz_h f_h(z_h - md) f_h(z_h) \right\} ,$$

33

$$H_{ij}^{\alpha\beta}(3) \equiv eF \sum_m \left\{ \left\langle \Phi_i^\alpha(m) \mid z_e \mid \Phi_j^\beta(0) \right\rangle - \left\langle \Phi_i^\alpha(m) \mid z_h \mid \Phi_j^\beta(0) \right\rangle \right\} \tag{2.51a}$$

$$\underset{closure}{=} eF \sum_m \sum_k A_k^{\alpha,i} A_k^{\beta,j} \int_{-\infty}^{\infty} dz_e f_e(z_e - (i+m)d) z_e f_e(z_e - jd) \int_{-\infty}^{\infty} dz_h f_h(z_h - md) f_h(z_h)$$

$$\tag{2.51b}$$

$$- \int_{-\infty}^{\infty} dz_e f_e(z_e - (i+m)d) f_e(z_e - jd) \int_{-\infty}^{\infty} dz_h f_h(z_h - md) z_h f_h(z_h) \ .$$

Though somewhat daunting in appearance, the matrix elements are easily accessible to a computational solution since all of the integrals over the along-growth-axis variables, z_e and z_h, are analytic. Of prime importance is that each of the terms contains a common factor of $C_{i,j}^{\alpha,\beta} \equiv \sum_k A_k^{\alpha,i} A_k^{\beta,j}$.

We see from the expression for $C_{i,j}^{\alpha,\beta}$ that in-plane states of different energy levels and different electron-hole along-axis separations are explicitly coupled in each matrix element of the SL Hamiltonian. Moreover we see that the coupling arises between in-plane basis states of like k and that all of the basis states contribute to some degree to this coupling. Simply put, the coupling between an in-plane state having energy index α calculated for an electron-hole separation id and an in-plane state having energy index β calculated for an electron-hole separation jd arises in a natural way as the inner product of their respective eigenvectors. We now discuss the construction of the Hamiltonian matrix, $\overleftrightarrow{H}_{SL}$.

As can be seen from the notation used for a matrix element, $H_{ij}^{\alpha\beta}$, the SL Hamiltonian depends on two sets of indices. The indices i and j are used to index the TW well locations with respect to the central period. We assign the index 0 to the central period of the superlattice. The indices α and β are used to index the different eigenstates of a give TW Hamiltonian. It is important to note that only a small subset of the available TW states need be included in the SL calculation. The number of TW states that are available equals the number of k-states used in the TW calculation. For the $R = 30a_0$ case we have a total of 300 TW states (for a given j) that can be used in the SL model. However, we only include 40 of these states in the SL calculation. The TW states that are not included are eigenstates that have energies that would place them well above the top of the SL miniband.

34

Assuming that we are including M TW states in the calculation, the matrix *element* corresponding to each pair of well indices, (i, j) , is a $M \times M$ submatrix, $\overleftrightarrow{S}_{i,j}$, that is indexed against the TW quantum numbers. When $i = j$, the orthonormality of the states being used in the model allows us to set $\overleftrightarrow{S}_{i,i} = \overleftrightarrow{I}$. Moreover, because of the symmetry of a type I lattice, we have that $\overleftrightarrow{S}_{-i,i} = \overleftrightarrow{S}_{i,-i} = \overleftrightarrow{I}$. Thus we see that the submatrices that lie on both the diagonal and anti-diagonal of the Hamiltonian are unit matrices. In the case of the off-diagonal submatrices we have that $\overleftrightarrow{S}_{i,j} = \overleftrightarrow{S}_{-i,j} = \overleftrightarrow{S}_{i,-j}$, again due to the symmetry of the lattice. Finally it is straightforward to show that $\overleftrightarrow{S}_{i,j} = \overleftrightarrow{S}_{j,i}^{T}$. Thus constructing the Hamiltonian requires the calculation of a few submatrices. The others can be assigned using the relations that we have shown here.

We now turn to our results.

35

Chapter 3

‟

Results and Analysis

In this chapter we present calculated absorption spectra for two $GaAs/Al_{0.3}Ga_{0.7}As$ superlattices having different periods, well widths and barrier widths. The parameters used for the calculations are given in Table I in Section 2.2. Unless otherwise specified, these parameters were used without any adjustments. Thus, for example, the exact absorption spectrum peak positions do not agree exactly with the locations of the experimental peaks. In light of the fact that experiments are subject to uncertainties in the applied electric field strengths and in the layer widths and compositions, it is often difficult to obtain precise agreement between experiment and theory in all aspects of the results. Thus, we have not attempted to adjust parameters to obtain better agreement with experiments. Rather, we have taken the author's numbers along with generally accepted material parameters and done no adjustments. Better agreement is likely possible if one is willing to adjust slightly many of the parameters, while still keeping them within acceptable bounds. However, as precise agreement with experiment was not the central aim of this work, this was not done here.

Prior to presenting our absorption results, we present, in Section 3.1, Table II, in which we compare the TW 1S exciton energies determined from our model with those determined using the Dignam & Sipe version. In Section 3.2 we present results for a superlattice having well widths of 67 Å and barrier widths of 17 Å (67/17). This superlattice was studied experimentally by Holdfel et. al [47] . We present separate graphs for each field strength presented in Figure 1 of Reference [47] . We also present graphs showing the absorption spectra for a wide range of applied static fields. In Section 3.3 we present results for a 40/40 superlattice and compare

36

Separation	DS 1S Exciton Energy (meV)	TW 1S Exciton Energy (meV)	Difference (meV)
0	65.85433917	65.77135114	0.082988034
1	70.36305097	70.21021822	0.152832754
2	71.97452371	71.85650343	0.118020277
3	72.69063302	72.59868233	0.091950689
4	73.10874285	73.03410027	0.074642581
5	73.38660983	73.32409026	0.062519566
6	73.58616212	73.53256254	0.053599582
7	73.7371333	73.69035499	0.046778317
8	73.85572156	73.81431564	0.041405925
9	73.95155952	73.91449387	0.03706565
10	74.03075875	73.99726272	0.033496037

Table 3.1: Comparison of the two-well 1S exciton energies. The separations are in units of superlattice period. The DS column gives the Dignam & Sipe results. The TW column gives the results from the model being presented.

these to the experimental results of Agulló-Rueda *et. al* [48] . Finally, in Section 3.4, we compare our model with other theoretical models from the literature.

3.1 Two-Well 1S Energies

Table 3.1 shows a comparison between calculated 1S exciton energies. The first column gives the along-the-growth-axis (z) separation between the electron and hole in units of the superlattice period for TW Hamiltonians of different electron-hole well separations, j . The second column contains the 1S exciton energy calculated using the Dignam & Sipe (DS) model [41] . We present our calculated energies in the third column. Finally, in the fourth column we show the differences in energy where we have subtracted our values from those from the DS model.

We see, from Table 3.1, that our results are slightly lower than those of DS. This indicates that the simple exponential function, used in references [39] and [40] , is a good variational wavefunction. Our energy results are slightly lower indicating a slight variational improvement. However, the point of the basis used here was not to get better 1S energy values, rather, it was to determine the higher in-plane states. In cases where the higher energy states can be ignored, considering the computational overhead included in calculating our TW states, using the DS model would be more efficient and would not significantly reduce accuracy.

37

3.2 The 67/17 Superlattice

Unless otherwise specified, the FWHM used in the calculation of the absorption spectra presented in the following figures was 2.5 meV. This was chosen to approximately match the experimentally measured FWHM of the 1S exciton peak in the absence of an applied field. The graphs show the absorption in arbitrary units as a function of photon energy in meV. The calculations were performed using 40 TW states. The TW states used were calculated at a radial extent of $30a_0$, using 300 basis states.

In Figure 3-1 we show a plot of the zero field absorption. This spectrum shows a 1S exciton peak rising at the lower edge of the combined electron-hole miniband and a broad, linearly rising plateau, attributable to the continuum states, that dips down to an essentially constant value near the upper combined-miniband edge. The broad absorption peak near 1595 meV and the dip immediately following it have been attributed to the lowest bound state resonance of the M1 saddle-point exciton [15][13] . The M1 saddle-point is a critical point that occurs near the top of the miniband. These critical points are characterized by masses having different signs along different directions of the band structure. The axial dispersion has a negative effective mass whereas the in-plane mass is positive at the M1 critical point [13] . Though the lineshape suffers from the energy-separation-induced oscillations at higher photon energies, as previously discussed in Section 2.2, we find that our calculated spectrum is in good agreement with the experimental absorption spectrum shown in Figure 1 of Reference [47] . We remind the reader that our work considers only heavy-hole excitons. The second peak, occurring at about 1569 meV in the experimental absorption, is attributable to a light-hole exciton. Thus, the small peak that can be seen at about 1571 meV in our absorption does not correspond to the one in the experimental graph. We note that the slope of the absorption between 1571 meV and 1595 meV agrees well with the experimental results, as does the relative absorption density in this range relative to the area under the 1S excitonic peak. The quick drop beyond 1595 meV, however, is clearly sharper in our calculated results than in the experimental one. This is likely due to the fact that we have not included light holes in our calculation.

38

Absorption Spectrum

F=0 kV/cm
R=30a$_0$
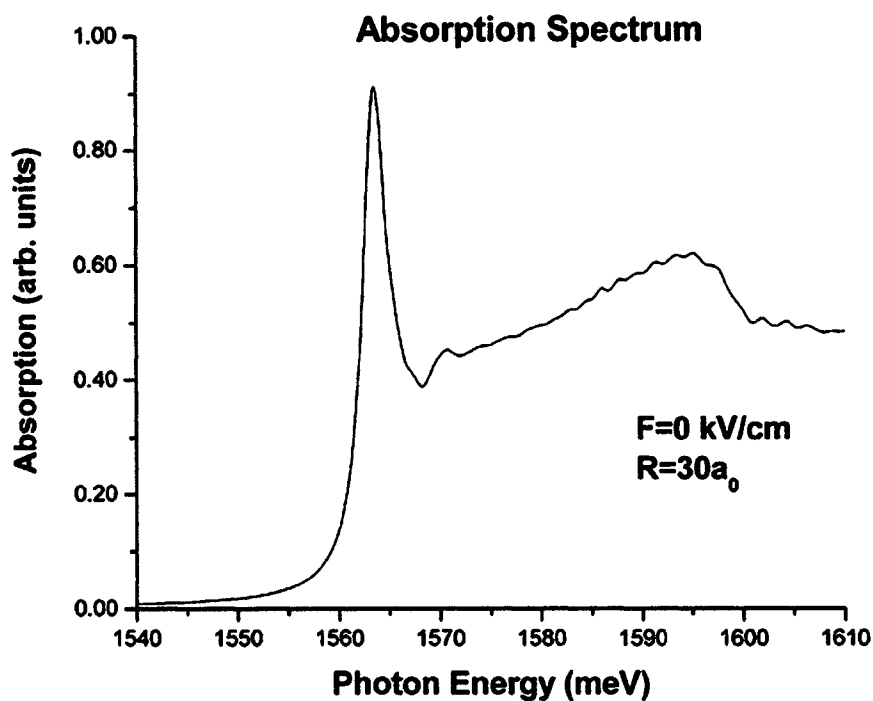
Figure 3-1: Zero-field absorption spectrum for the 67/17 superlattice calculated using 40 TW states having an in-plane radius of 30a$_0$. This spectrum agrees very well with the experimental results of Holfeld $et.$ $al.$

We are able to clearly identify the sharp absorption peak in the spectrum of Figure 3-1 as the 1S absorption peak. However, once an electric field is applied, all of the 1S states are coupled to the continuum states of lower energy WSL states. However, as these states are predominately 1S in character, for the purposes of discussion we shall refer to these peaks as "1S peaks" in what follows.

In Figure 3-2 through Figure 3-4 we show our calculated absorption for applied static fields of 9.1 kV/cm, 13.3 kV/cm and 15.5 kV/cm respectively. We find that these predicted spectra have a reasonable agreement with the experimental results of Figure 1 in Reference [47] . Clearly evident are the WSL peaks in each of these plots. Where possible, the 1S-like excitonic peaks are labelled by the appropriate WSL index. However, for the field of 9.1 kV/cm, the Coulomb effects result in such strong mixing that such a designation is not possible. We also see the

39

typical signature of Fano coupling in the shape of most of the 1S-like WSL peaks. The dips below the continuum absorption occurring at energies just above the 1S-like WSL peaks are easily recognized in each of the absorption lineshapes presented in these three figures. Also evident is the asymmetry in the peak shapes due to their extension to lower energies. These features were discussed extensively in Holfeld *et. al* [47] . Finally we note that these plots all preserve the rise of the background absorption due to the continuum states.

Absorption Spectrum
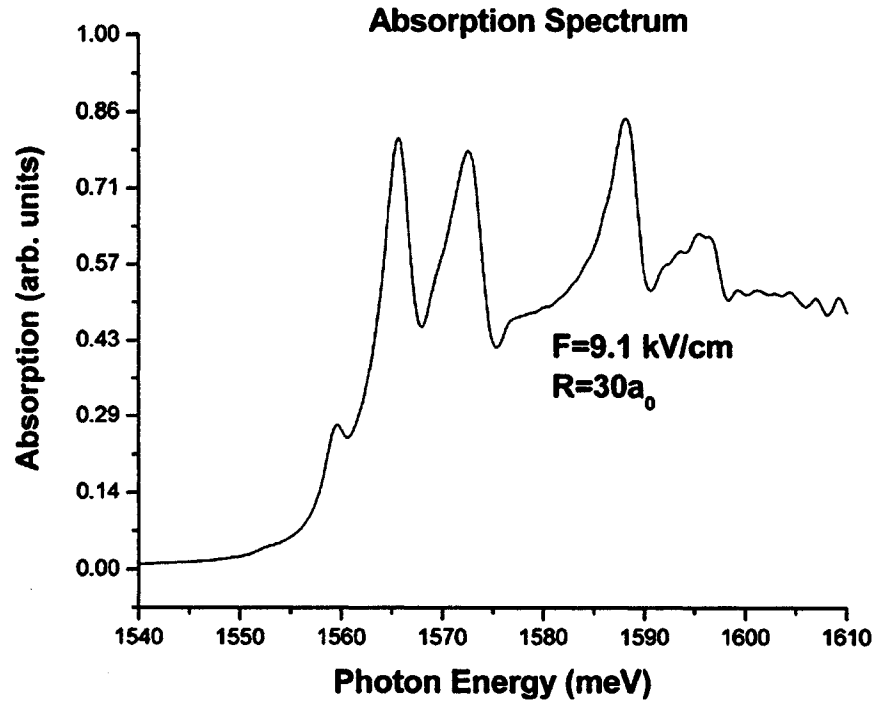
F=9.1 kV/cm
R=30a$_0$

Figure 3-2: Absorption spectrum for the 67/17 superlattice subject to an applied field of 9.1 kV/cm.

40
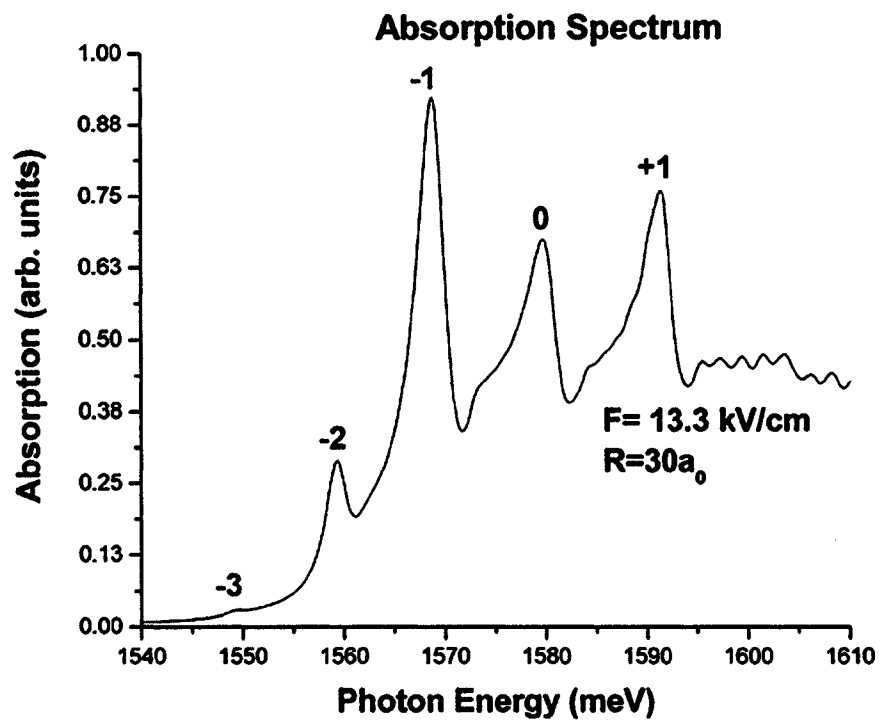
Figure 3-3: Absorption spectrum for the 67/17 superlattice subjected to a 13.3 kV/cm static field.

41

Absorption Spectrum
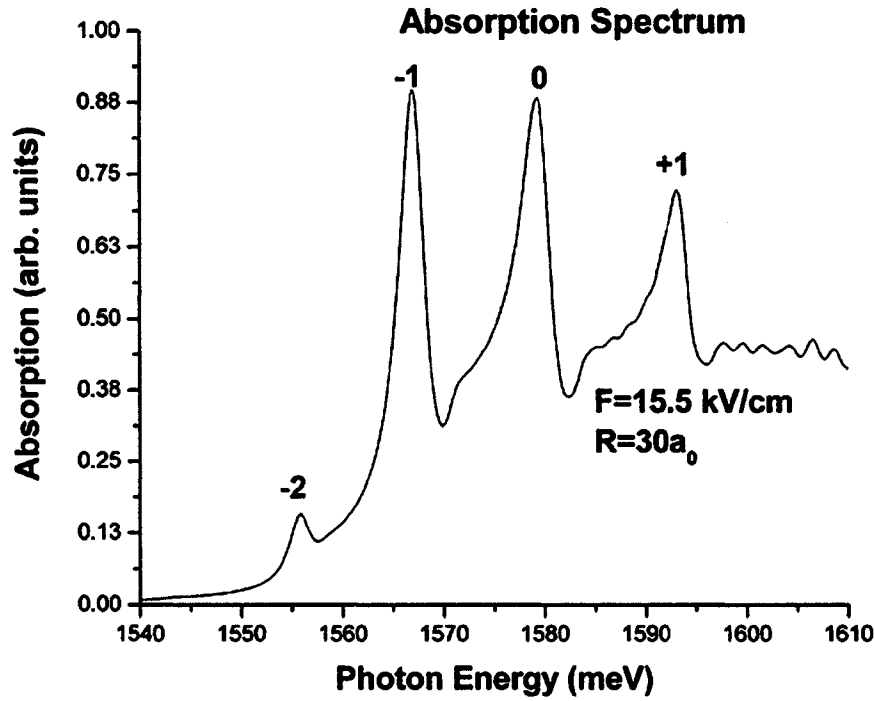
Figure 3-4: Absorption spectrum for the 67/17 superlattice subject to an applied field of 15.5 kV/cm.

Before returning to our comparisons with the experimental results presented in Figure 1 of Reference [47] we turn to a comparison of the spectrum presented in Figure 3(a) of the same paper. The differences in scale between the aforementioned Figure 1 and our calculated results can make a direct comparison somewhat difficult. Figure 3(a) on the other hand would seem to be on a similar scale to that which we have used. Figure 3-5 shows our calculated absorption spectrum for an applied field of 16.7 kV/cm. Though a comparison with Figure 3(a) of reference [48] suggests that the model has overestimated the magnitude of the peak at 1584 meV, we find that our theoretical spectrum otherwise makes an excellent match with the one in Figure 3(a). Our model correctly predicts the magnitude and effect of the Fano resonance induced asymmetry towards lower energy. It also provides comparable values for the depth and widths of the Fano dips on the high energy side of the WSL peaks. We note that direct comparison is further complicated by the fact that the composition, electric field and lattice period used in

42

the experiments are never exactly known and the relative peak heights are sensitive to these factors.

Absorption Spectrum
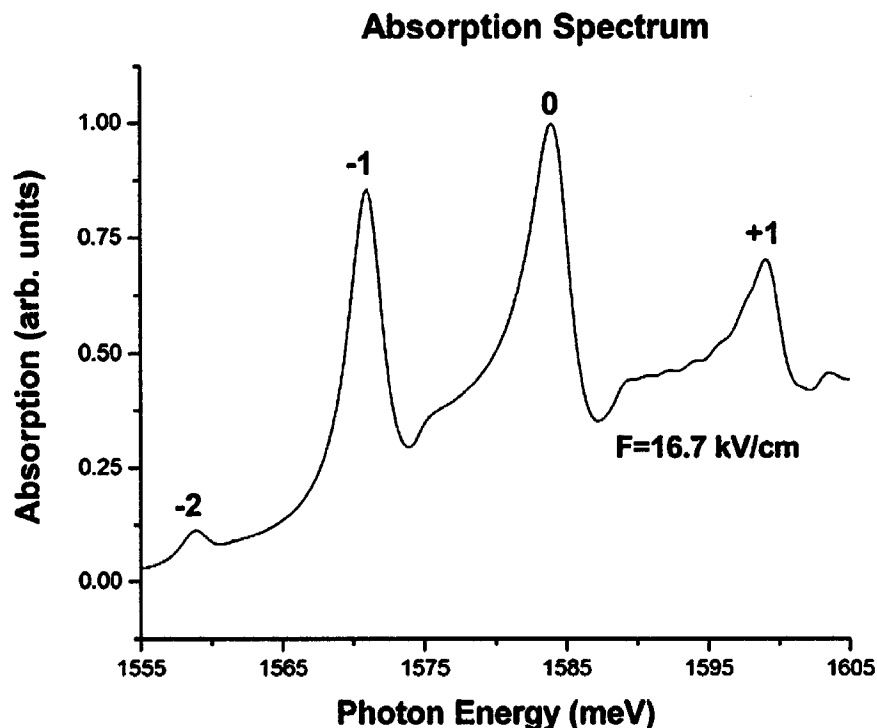
Figure 3-5: Absorption spectrum for the 67/17 superlattice with an applied field of 16.7 kV/cm. Other than an over-estimation of the magnitude of the central peak, this spectrum is in excellent agreement with the experimental spectrum given in Figure 2 of reference [47] .

Figure 3-6 is our final plot for comparison to the results in Figure 1 of reference [47] . We see that our spectrum again compares reasonably well to the experimental results. Our clearly defined WSL peaks exhibit the typical Fano resonance behaviour and the background due to the continuum states is evident in the plot. Though the peaks in our calculated results do not fall exactly on the same lines as the experimental ones, we find that the field-induced separations of the peaks are essentially the same. Again, we see a fairly strong discrepancy in the relative magnitudes of the absorption peaks. We are not certain of the cause of this.

43

Absorption Spectrum
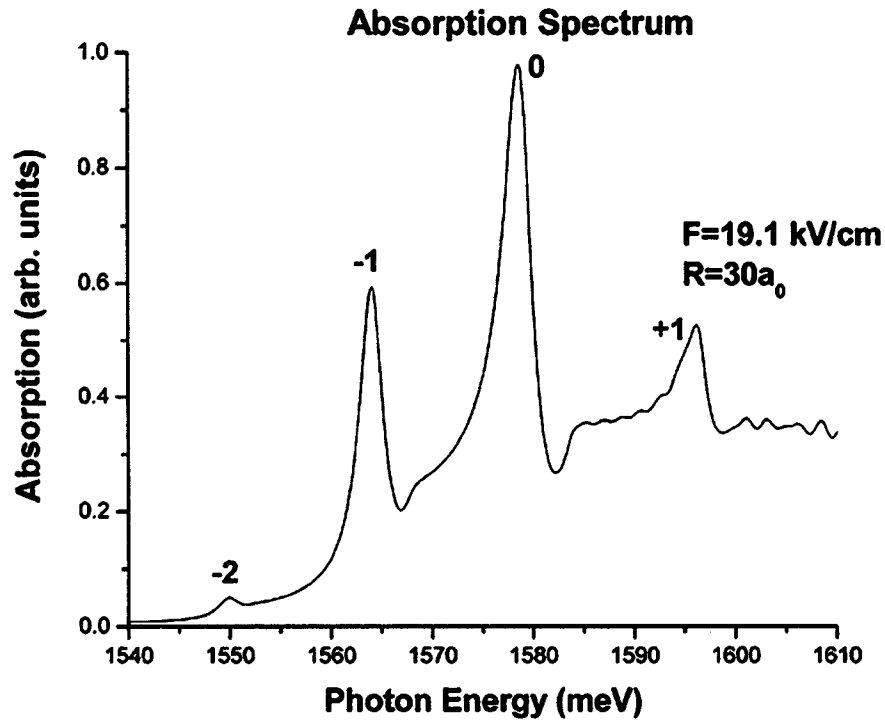
Figure 3-6: Absorption spectrum for the 67/17 superlattice subject to an applied field of 19.1 kV/cm.

Figure 1 in Holfeld *et. al* shows theoretically determined spectra along with the experimental ones. According to the authors, these theoretical spectra were calculated using the model in Whittaker [13] . It would appear that , in the zero field case, the Whittaker model only predicts the 1S-like excitonic peak whereas, as seen in Figure 3-1, our model provides the full spectrum. For the remaining spectra however, the Whittaker model does a better job in predicting the relative magnitudes of the 1S-like excitonic peaks whereas our model provides a more accurate picture of the rise due to the continuum states. We are not certain of the source of these discrepancies.

In Figure 3-7 we show a waterfall plot of absorption spectra for applied fields ranging from 0 kV/cm to 40 kV/cm. For field strengths $\gtrsim$ 10 kV/cm, the WSL transitions are easily resolved. The dip and asymmetry of peak shape can clearly be seen in the dominant peak. We also see the rise of a background plateau due to the quasi-continuum states. Inset is an image plot of

44

the same data. The familiar fan shape of the WSL can be seen in the image. The colour scheme used combines orange for the weakest absorption shading to black at the maximum calculated value. The dark black line in the centre of the image corresponds to the dominant peak. We can also see a bright orange stripe to its immediate right indicating the Fano resonance dip. Looking to the right of the other black lines that indicate the WSL transitions, we see a similar orange stripe due to Fano resonances at these transitions. We note that the oscillations that are evident in the continuum plateau are an artifact caused by the energy separations between the quasi-continuum states in our basis.
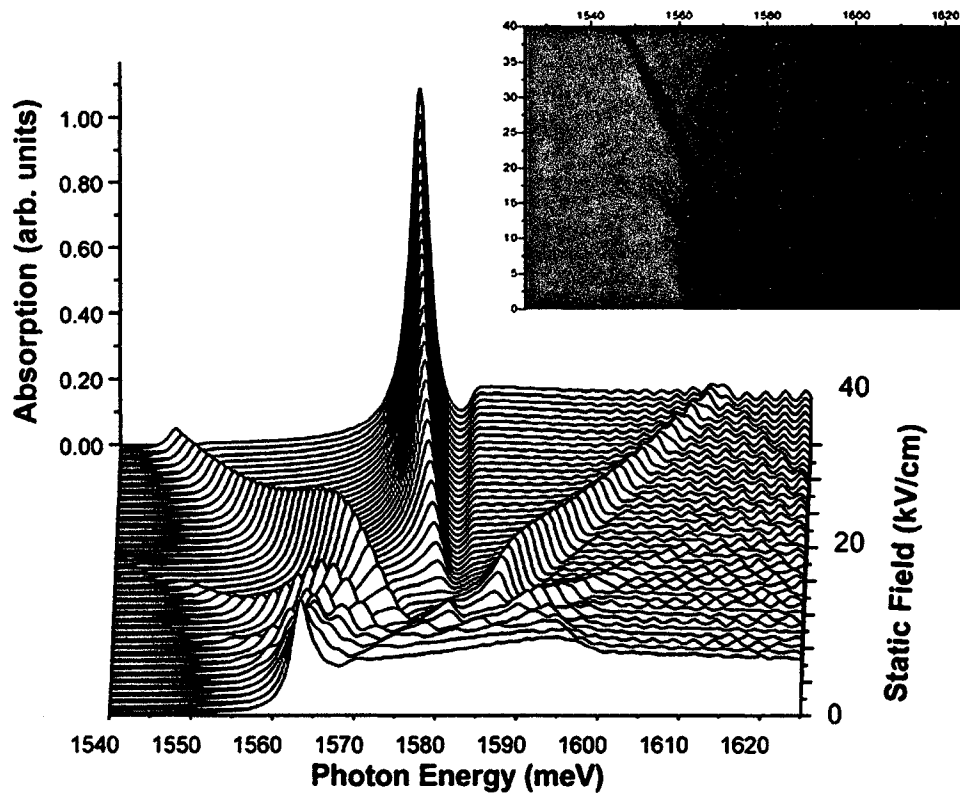
Figure 3-7: Absorption spectra for the 67/17 superlattice for fields from 0 kV/cm to 40kV/cm. Inset is an image map of the data where the vertical axis is the field strength and the horizontal axis is the photon energy. The familiar fan-shape of the WSL is clearly evident.

Our next series of spectra cover a reduced range of applied fields. Figure 3-8 shows a waterfall plot for applied fields from 0 kV/cm to 12 kV/cm. Figure 3-9 is an image map of the data from Figure 3-8.

45

Zero to Mid-Field Absorption
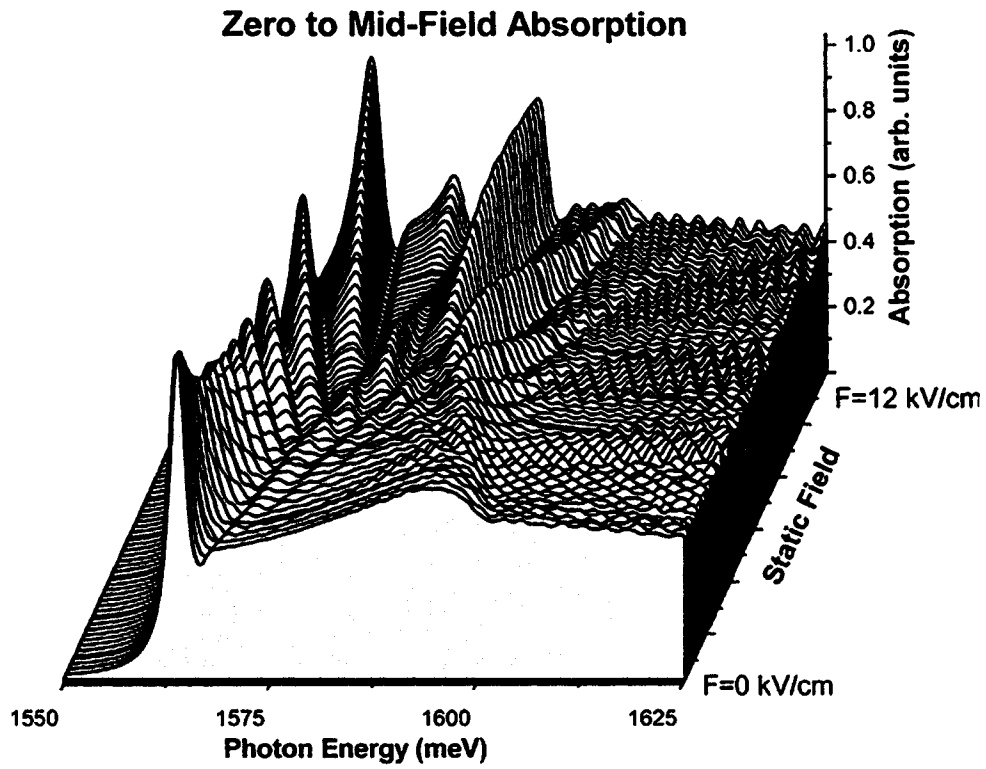
Figure 3-8: Absorption spectra for the 67/17 superlattice for applied fields ranging from 0 kV/cm to 12 kV/cm. The plot shows spectra calculated at 1 kV/cm increments.

46
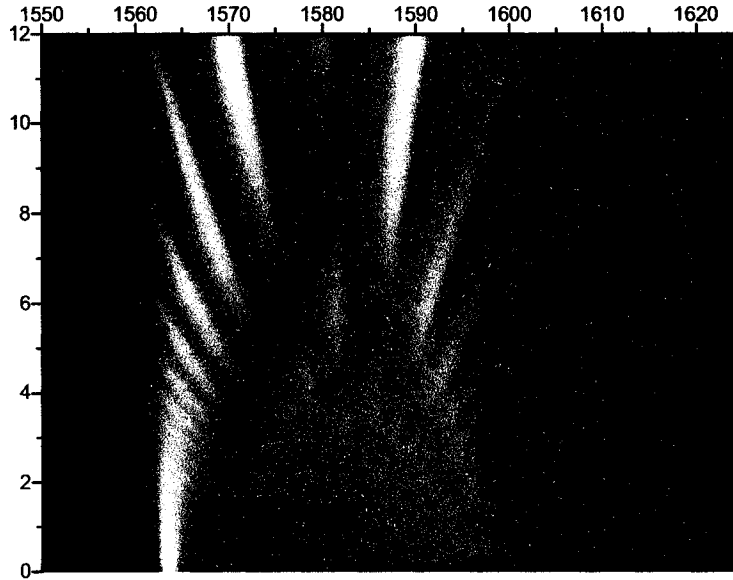
Figure 3-9: Image map for Figure 3-8. The horizontal axis is the photon energy in units of meV and the vertical axis is the field strength in units of kV/cm.

Figures 3-8 and 3-9 clearly show the crossings of the negative WSL states with the 0th state and the oscillations in the absorption of the individual WSL states. The series of diagonal lines between 1555 meV and 1575 meV are evidence of the anti-crossing behaviour between the WSL states of negative index and the zeroeth state. The oscillation in the absorption of the zeroeth state (near 1580 meV) can be seen most clearly in the image map, Figure 3-9. The first indication of this state's absorption can be seen at an energy of about 1584 meV for a 3 kV/cm field. A succession of peaks and troughs occur with increasing field. Troughs occur between ~3.5 to 4.5 kV/cm and again between ~8 to 10.5 kV/cm. Both of these effects are extensively discussed in Dignam & Sipe [39] . The triangular structure of evenly spaced (for a given field strength) peaks that occurs between 1565 meV and 1595 meV for fields form ~2 kV/cm to ~8 kV/cm result form a combination of the level anti-crossings and the oscillatory absorption of a given WSL state. Similar structure can be seen in Figure 6 of Linder [15] .

We complete this section with Figure 3-10, which shows a plot of absorption spectra for fields from 1 kV/cm to 8 kV/cm, where the spectra have been calculated for field increments

47

of 0.05 kV/cm and Figure 3-11, which is the image map for Figure 3-10. These plots provide
higher resolution images of the structures described above in conjunction with Figures 3-8 and
3-9.

**High Resolution Low Field
Absorption Spectrum**
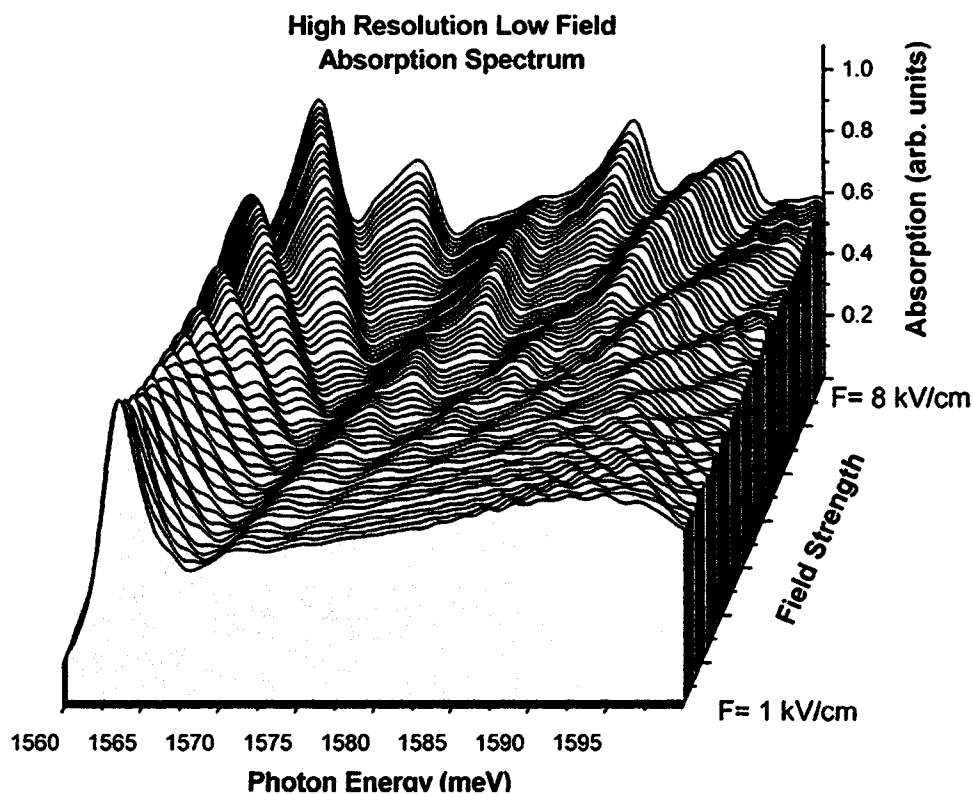
Figure 3-10: Absorption spectra for fields from 1 kV/cm to 8 kV/cm in increments of 50
V/cm. Anti-crossings of WSL states of negative index with the zeroeth state is clearly
identifiable. Also seen is the absorption oscillation of the zeroeth state and the interaction
between this oscillation and the anticrossings.

48
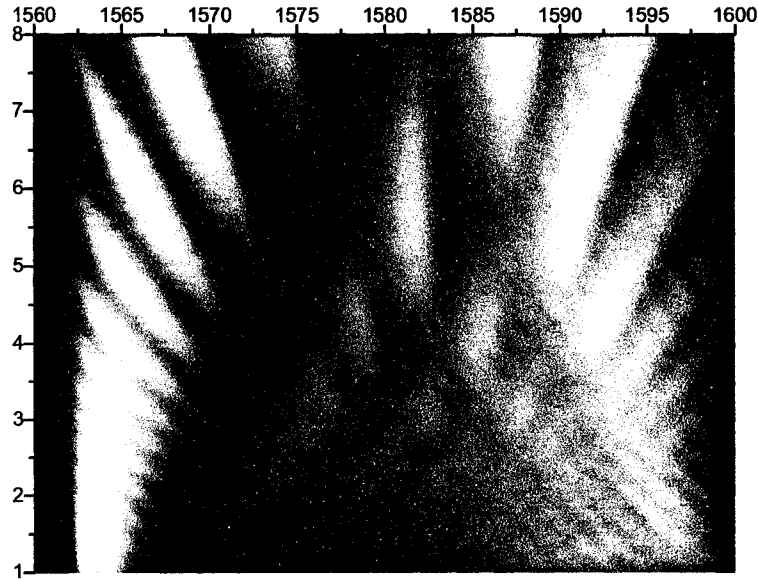
Figure 3-11: Image map of the data from Figure 3-10.

3.3 The 40/40 Superlattice

In Figure 3-12 to Figure 3-14 we present calculated absorption spectra for a superlattice having equal well and barrier widths of 40 Å. We compare these results to the experimental results presented in reference [48] . The TW basis used here consisted of 50 states calculated at an in-plane radial extent of $30a_0$ using 300 in-plane basis states.

Figure 3-12 shows our calculated spectrum for an applied field of 10 kV/cm. Despite an exaggerated separation between the peaks at 1640 meV and 1650 meV that can be attributed to the FWHM used in our calculation we find an excellent match between our results and the experimental results presented in Figure 1 of reference [48] . Again, since are only considering heavy-hole excitons, our spectrum does not show the experimental light-hole peaks.

49

Absorption Spectrum
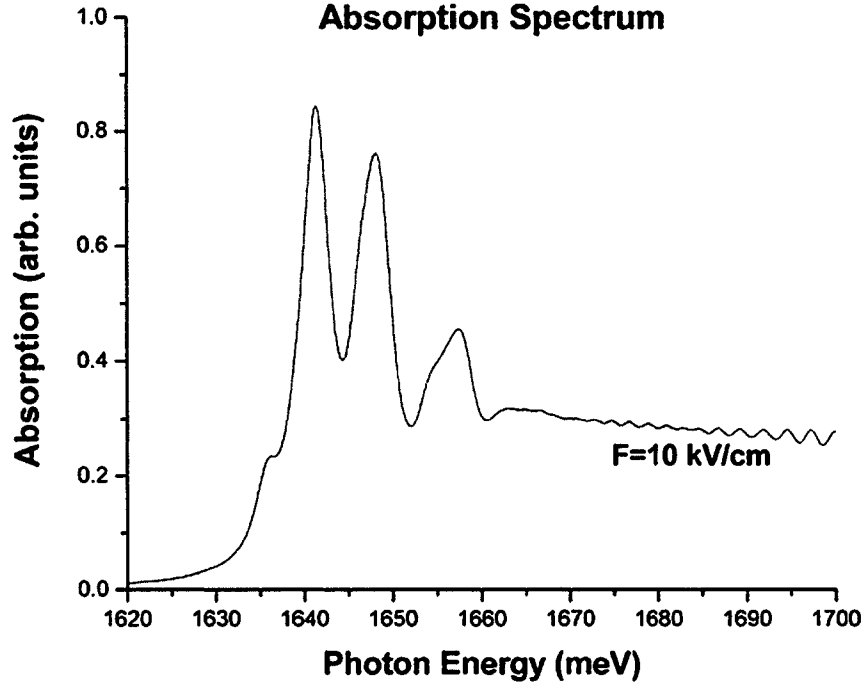
Figure 3-12: Absorption spectrum for the 40/40 superlattice subject to an applied field of 10 kV/cm.

Figure 3-13 shows our calculated absorption spectrum at 40 kV/cm. This result an excellent match to the result present in Figure 1 of reference [48] for the same field strength (omitting the light-hole peaks). We see here a spectrum that resembles the zero-field result of the 67/17 lattice. This can be understood in a relatively straightforward way by considering the effect of a strong field on the inter-well coupling in this superlattice. When the field is strong, this coupling is very weak and the wavefunctions will be essentially completely localized within the given wells. This arises because the barrier widths along with the field induced energy shift effectively negate any probability of inter-well tunneling. Hence, for fairly wide barriers that have the same widths as the wells we get an absorption profile similar to that of a single well.

50

Absorption Spectrum

F=40 kV/cm

Photon Energy (meV)

Absorption (arb. units)
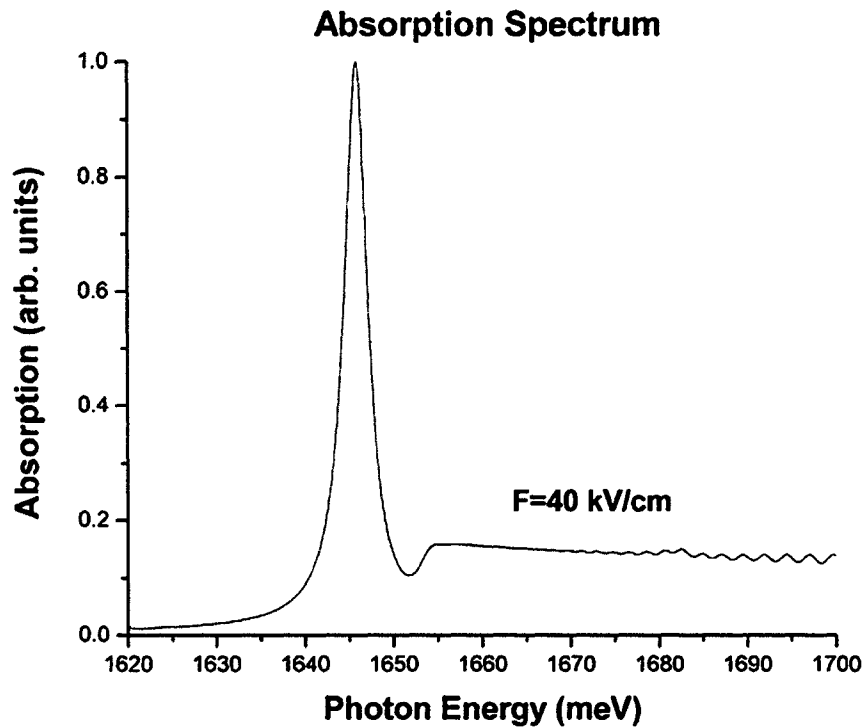
Figure 3-13: Absorption spectrum for the 40/40 superlattice subject to an applied field of 40 kV/cm. We find excellent agreement with the results of Agulló-Rueda *et. al.* [Phys. Rev. B **41**,1676 (1990) Figure 1].

Figure 3-14 shows the evolution of the absorption spectra for the 40/40 lattice as the applied field is increased from 0 kV/cm to 40 kV/cm. We can see a weak WSL that is strongest at medium field strengths and that all but disappears as the field approaches 40 kV/cm. The weakness of the WSL can be attributed to a reduction in inter-well tunnelling arising due to the width of the barriers. The non-linear shift towards lower energies for $7 \lesssim F \lesssim 14$ kV/cm is due to the Coulomb mixing of the 0 and -1 1S-like states, as has been discussed by Dignam & Sipe [39] . The inset image map clearly shows the weakness of the WSL transitions in this structure.

51

Absorption Spectra
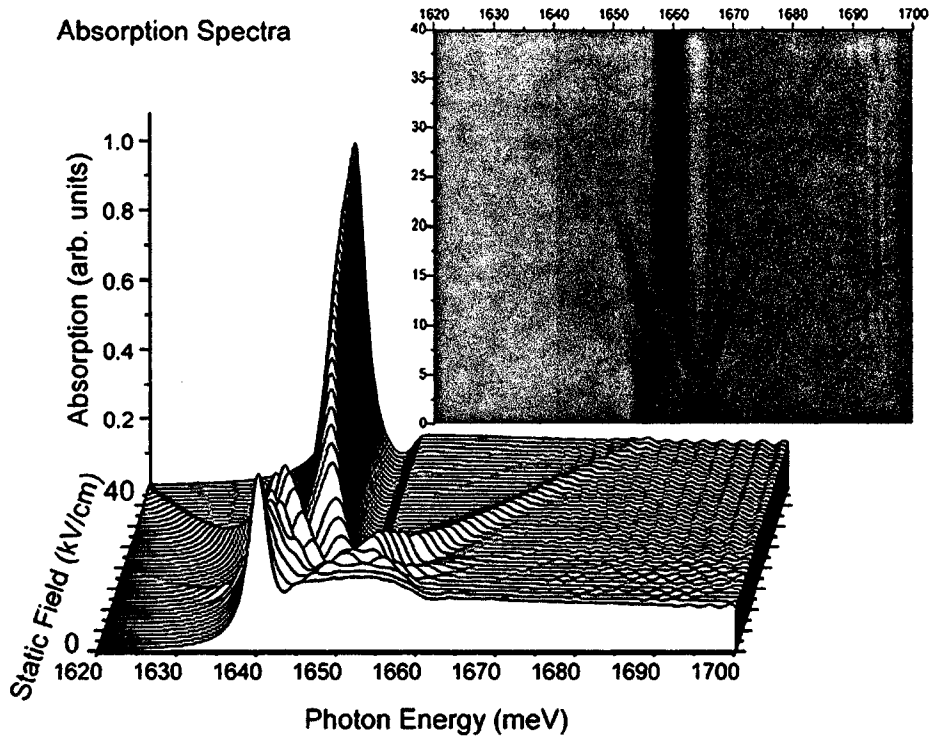
Figure 3-14: Absorption spectra for the 40/40 superlattice at field strengths ranging from 0 kV/cm to 40 kV/cm. A weak WSL is clearly evident.

52

Chapter 4

Conclusion

In summary, we have presented an excitonic model for type-I superlattices that is based on the work of Dignam & Sipe. The model determines the superlattice wavefunctions by expanding the excitonic Hamiltonian in an excitonic Two-Well basis that includes both bound and quasi-continuum states. The optical absorption spectra calculated using this theoretical model are in very good agreement with experimental results over a wide range of field strengths. In practice, the model requires two sets of computational calculations. The first determines the two-well states that are used in the second, the superlattice calculation. We conclude with a discussion of the advantages and disadvantages of the method.

The two-well calculation uses a single in-plane basis index k as opposed to the oft used k_x, k_y component indexing, simplifying the calculations. This provides the additional advantage of giving the correct rotational symmetry without requiring extra work. The description used for the two-well states leads to a relatively simple calculation of the Coulomb interaction between the electron and the hole. In terms of computation however, this calculation is a limiting factor with respect to the time required to generate the two-well states for a given along-axis electron-hole separation. A major disadvantage to the two-well in-plane basis is that the higher energy continuum states become further apart with increasing k , leading to incorrect oscillations at higher photon energies in the calculated superlattice absorption lineshapes. This will be a problem in any calculation using a basis of eigenstates of a finite system. A lesser disadvantage is the number of basis states required to accurately represent the two-well states. These can be as few as 300 to as many as 600 or more. This is a small number when compared to what was

53

reported above in the case of the single-particle model ([24],[28]) . The required calculation can take a up to a day to generate eigenvectors and eigenenergies for a single electron-hole along-axis separation using a dual-processor (500 MHz) alpha workstation containing 2 Gb of RAM. This means that for a superlattice consisting of $2N + 1$ periods, it can take as long as about $N + 1$ days to generate the necessary two-well states. However, once a given set of two-well states are generated, they can be used in the superlattice calculation at all field strengths. Since we use the two-well states as a basis for the superlattice problem we can choose to use a small subset of the available states. The SL calculations themselves however take little time to compute. A given spectrum at a single field, as shown in the plots above, takes about 2 hours to complete on a basic Pentium 4, 1.6 Ghz clone containing 256 Mb RAM.

Other than the aforementioned oscillations in the absorption spectra at high energies, we find excellent agreement with experimental results at all field strengths. Moreover, the orthonormality of the two-well eigenstates for a given separation leads to expressions for the superlattice Hamiltonian matrix elements that are quickly determined. This also leads to fairly simple expressions for the absorption coefficients. The relative ease of calculation of the superlattice Hamiltonian and of the quantities of interest leads to a computation that can provide complete superlattice information on a relatively short time scale (~hours) . This efficiency is critical when the results provided by the model are to be subsequently used in further calculations. For example, when calculating the excitonic dynamics of a superlattice, it is necessary to calculate intraband dipole matrix elements $\mathbf{G}_{\nu\mu} \equiv \langle \psi^{\nu} | -e (\mathbf{r}_e - \mathbf{r}_h) | \psi^{\mu} \rangle$ where ψ^{ζ} is the ζth superlattice excitonic eigenstate [14] . Efficient and accurate representations of the superlattice wavefunctions are imperative to such a calculation. Moreover, it can be seen in reference [14] , that accurate estimates for the energy of each of these states are also required.

4.1 Suggestions for Further Study

The model discussed here includes only the lowest electron and hole minibands imposing a minimum width constraint on the wells of the superlattice. Extending the model to include higher energy minibands would expand the capabilities of the model to a wider variety of superlattices and allow us to examine the effects on interband coupling.

54

Secondly, the inclusion of the light-hole sub-band would provide an opportunity to explore the mixing effects between light- and heavy-hole excitons. This would also provide the ability to make more direct comparisons with experimental spectra.

55

Chapter 5

Appendices

5.1 Appendix A: Determination of R (in-plane radial extent) and N_R (# of included k-states)

We have as yet to determine an analytical expression that would provide an estimate for the optimal finite radial extent that should be used in the determination of the TW states. The same can be said about the number of k-states to include for a given radius. However, as a "rule of thumb", a good starting point for the number of k-states is to include a number equal to 10 times the radial extent in units of a_0. To date, all determinations have been made by running the calculation for a given set of parameters and then checking against the criteria stated in the Two Well section of the chapter on theory. Our experimentation with the program has shown that estimates for the bound state energies improve with increasing R and that the separation between the energies of the quasi-continuous states decrease simultaneously. Tied to the decrease in energy separations is an increase in the number of quasi-continuous states that are generated over a given energy range.

In Table A-1, we compare the energies of the bound two-well eigenstates determined using $R = 40a_0$ and $N_R = 400$ with those determined using $R = 30a_0$ and $N_R = 300$. All energies are given in meV.

	$R = 30a_0$, $N_R = 300$		$R = 40a_0$, $N_R = 400$	
	Total Energy (meV)	Binding Energy (meV)	Total Energy (meV)	Binding Energy (meV)
1S	65.79	-9.15	65.79	-9.15
2S	73.56	-1.38	73.56	-1.38
3S	74.41	-0.53	74.41	-0.53
4S	74.68	-0.26	74.66	-0.28
5S	74.93	-0.02	74.80	-0.14

We see here that both sets of parameters return eigenstates with the same energy values for the 1S through 3S states. However, in analogy to a variational calculation, we find that the $R = 40a_0$ results provide both more accurate estimates for the 4S and 5S energies, and a smaller separation between the energies of these two states. Our testing to date has returned at most 5 bound states. This is because we are referencing to an unbound ($R = \infty$) free pair and for $n > 4$ the kinetic energy associated with the confinement to a finite disk is larger than the Coulomb energy.

In the following figure we plot the energy differences as a function of state number for the quasi-continuous states of both the $R = 40a_0$, $N_R = 400$ and $R = 30a_0$, $N_R = 300$ runs. The legend in the figure identifies these as R=40 and R=30 respectively. Included in the figure are plots of the energy differences as determined by using an asymptotic expansion. In the limit of large k, we can write

$$J_0(kR) = \sqrt{\frac{2}{\pi kR}} \cos(kR - \pi/4),$$

and

$$J_1(kR) = \sqrt{\frac{2}{\pi kR}} \cos(kR - 3\pi/4).$$

Using these expansions, it is straightforward to show that eigenvalues for the Bessel functions

57

become

$$k_n R = (n + 3/4)\,\pi.$$

Thus we find that the energies for these states become

$$
\begin{aligned}
E_{k_n} &= \frac{\hbar^2 k_n^2}{2\mu} \\
&= \frac{\hbar^2 \left(n + 3/4\right)^2 \pi^2}{2\mu R^2}.
\end{aligned}
$$

Thus the energy differences in the asymptotic limit of large k are

$$
\begin{aligned}
\Delta E_n &\equiv E_{k_n} - E_{k_{n-1}} \\
&= \frac{\hbar^2 \pi^2}{2\mu R^2} \left(2n + \frac{1}{2}\right).
\end{aligned}
$$

Quasi-Continuum Energy Differences
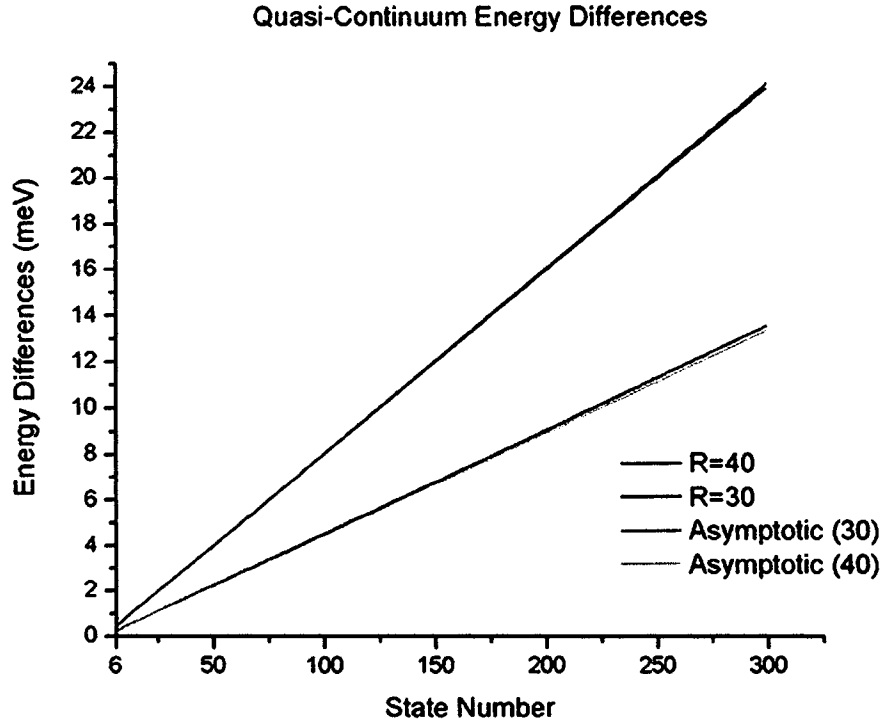
Figure A-1: Energy differences between the quasi-continuous states as a function of state number are plotted for in-plane radii of $30a_0$ and $40a_0$. These are compared to energy difference lines determined by asymptotic expansions at the same radii. The $30a_0$ calculation was performed using 300 k-states. 400 k-states were used in the $40a_0$ calculation. Only state numbers up to 300 are shown.

We see that both the $R = 30a_0$ energy difference line and the line for $R = 40a_0$ have essentially converged to the difference lines determined from the asymptotic expansion for these radii respectively. Thus the asymptotic expansion provides us with a method by which we can predict the energy difference between eigenstates. This allows the prediction of the radius required to minimize oscillations at a given Lorentzian FWHM.

The final figure in this appendix shows the purely 2D absorption spectrum in the absence of Coulomb interaction for a single well. The absorption calculations were performed using a Lorentzian FWHM of 2.0 meV for the two cases that we have been discussing in this appendix.

59

Absorption Spectra
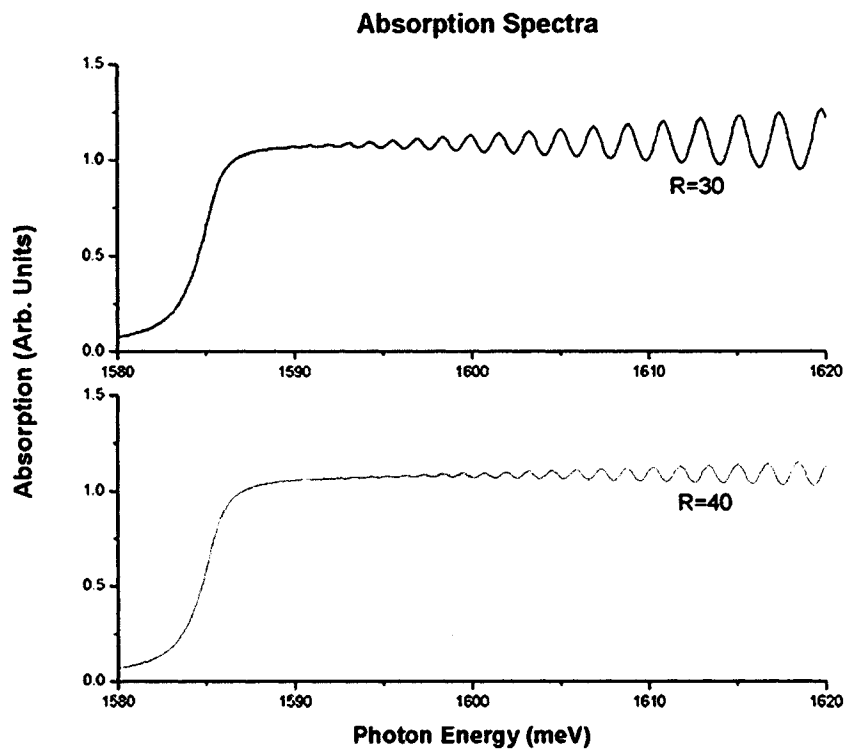
Figure A-2: Comparison of the strictly 2D absorption lines, in the absence of Coulomb interaction, for radii of $R = 40a_0$ and $R = 30a_0$. A significant improvement can be seen in the R=40 lineshape.

The oscillations in the lineshapes are due to energy separations between the continuum states that are greater than the Lorentzian FWHM. A significant reduction in the number of oscillations and their magnitude can be seen in the $R = 40$ plot.

60

Bibliography

[1] F. Bloch, Z. Phys., **52**, 555 (1928).

[2] J. Feldmann, K. Leo, J. Shah, D.A.B. Miller, J.E. Cunningham, T. Meier, G. von Plessen, A. Schulze, P. Thomas, and S. Schmitt-Rink, Phys. Rev. B, **46**, 7252 (1992).

[3] G. H. Wannier, Phys. Rev., **117**, 432 (1960).

[4] Hubert M. James, Phys. Rev., **76**, 1611 (1949).

[5] L. Esaki and R. Tsu, IBM J. Res. Dev., **14**, 61 (1970).

[6] These early structures had a large number of imperfections.

[7] E. E. Mendez,G. Bastard, L. L. Chang, L. Esaki, H. Morkoç, and R. Fischer, Phys. Rev. B, **26**, 7101 (1982).

[8] R. C. Miller and A. C. Gossard, Appl. Phys. Lett., **43**, 954 (1983).

[9] T. H. Wood, C. A. Burrus, D. A. B. Miller, D. S. Chemla, T. C. Damen, A. C. Gossard, and W. Wiegmann, Appl. Phys. Lett., **44**, 16 (1984).

[10] D. A. B. Miller, D. S. Chemla, T. C. Damen, A. C. Gossard, W. Wiegmann, T. H. Wood, and C. A. Burrus, Phys, Rev. Lett., **53**, 2173 (1984); *ibid.*, Phys. Rev. B, **32**, 1043 (1985).

[11] E. E. Mendez, F. Agulló-Rueda, and J. M. Hong, Phys. Rev. Lett., **60**, 2426 (1988).

[12] V. G. Lyssenko, G. Valušis, F. Löser, T. Masche, K. Leo, M. M. Dignam, and K. Köhler, Phys. Rev. Lett., **79**, 301 (1997).

[13] D. M. Whittaker, Europhys. Lett., **31**, 55 (1995).

[14] J.M. Lachaine, Margaret Hawton, J.E. Sipe and M.M. Dignam, Phys. Rev. B, **62**, R4829 (2000).

[15] N. Linder, Phys. Rev. B, **55**, 13664 (1997).

[16] U. Fano, Phys. Rev., **142**, 1866 (1961).

[17] J. Zak, Phys. Rev. Lett., **20**, 1477 (1968).

[18] Any reference list for this topic would necessarily be incomplete. Noteworthy examples are: J. Bleuse, G. Bastard, and P. Voisin, Phys. Rev. Lett., **60**, 220 (1988); J. Callaway, Phys. Rev., **130**, 549 (1963). For a general treatment of periodic media see reference [20] .

[19] See, for example: J. Rotvig, A.-P. Jauho, and H. Smith, Phys. Rev. Lett., **74**, 1831 (1995); D. W. Hone and X.-G. Zhao, Phys. Rev. B, **53**, 4834 (1996).

[20] Paula Feuer, Phys. Rev., **88**, 92 (1952).

[21] See, for example, J.M. Ziman in *Principles of the Theory of Solids*, 2nd Ed. (Cambridge University Press, London, 1972) page 191 ff.

[22] Reference [21] , page 194.

[23] D. Emin and C. Hart, Phys. Rev. B, **36**, 7353 (1987); L. Kleinman, *ibid.*, **41**, 3857 (1990); D. Emin and C. Hart, *ibid.*, **41**, 3859 (1990); D. A. Brown and E. Brown, *ibid.*, **43**, 2423 (1991); J. Zak, *ibid.*, **43**, 4519 (1991); J. Leo and A MacKinnon, *ibid.*, **43**, 5166 (1991).

[24] S. Glutsch, D. S. Chemla, and F. Bechstedt, Phys. Rev. B, **54**, 11592 (1996).

[25] S. Glutsch and F. Bechstedt, Phys. Rev. B, **57**, 11887 (1998).

[26] S. Glutsch and F. Bechstedt, Phys. Rev. B, **60**, 16584 (1999).

[27] H. Chu and Y.-C. Chang, Phys. Rev. B, **36**, 2946 (1987).

[28] H. Chu and Y.-C. Chang, Phys. Rev. B, **39**, 10861 (1989).

[29] W. T. Masselink, P. J. Pearah, J. Klem, C. K. Peng, H. Morkoç, G. D. Sanders and Y.-C. Chang, Phys. Rev. B, **32**, 8207 (1985).

[30] A. Chomette, B. Lambert, B. Deveaud, F. Clerot, A. Regreny, and G. Bastard, Europhys. Lett., **4**, 461 (1987).

[31] G. Mo and C. C. Sung, Phys. Rev. B, **38**, 1978 (1988).

[32] S. Glutsch and F. Bechsetdt, Phys. Rev. B, **54**, 11592 (1996).

[33] D. M. Whittaker, Phys. Rev. B, **41**, 3238 (1990).

[34] G. H. Wannier, Phys. Rev., **52**, 191 (1937).

[35] See, for example, M. Altarelli in *Interfaces, Quantum Wells, and Superlattices*, edited by C. Richard Leavens and Roger Taylor (Plenum, New York, 1988).

[36] See, for example, Gerald Bastard, *Wave Mechanics applied to Semiconductor Heterostructures*, (Halsted Press, New York, 1988) chpt. II.

[37] U. Ekenberg and M. Altarelli, Phys. Rev. B, **35**, 7585 (1987).

[38] G. D. Sanders and Y. C. Chang, Phys. Rev. B, **31**, 6892 (1985).

[39] M.M. Dignam and J. E. Sipe, Phys. Rev. B, **43**, 4097 (1991).

[40] M.M. Dignam and J.E. Sipe, Phys. Rev. B, **41**, 2865 (1990).

[41] Values provided by Marc Dignam in private correspondence.

[42] See, for example, Hartmut Haug and Stephan W. Koch, *Quantum Theory of the Optical and Electronic Properties of Semiconductors*, (World Scientific, Signapore, 1998) chpt. 10.

[43] See, for example, C. Cohen-Tannoudji, B. Diu, and F. Laloe, *Quantum Mechanics*, (Hermann, Paris, 1977), Chapter 1.

[44] See, for example, Neil Ashcroft and N. David Mermin, *Solid State Physics*, (Holt, Rinehart & Winston, New York, 1976).

[45] See, for example, John David Jackson, *Classical Electrodynamics*, 3rd ed. (Wiley, New York, 1999).

[46] See, for example, Ref. [36] chpt. VI, § II.2.

[47] C.P. Holfeld, F. Löser, M. Sudzius, D.M. Whittaker, and K. Kohler, Phys. Rev. Lett., **81**, 874 (1998).

[48] F. Agulló-Rueda, J.A. Brum, E.E. Mendez, and J.M. Hong, Phys. Rev. B, **41**, 1676 (1990).

[49] See, for example, references [47] and [48] .